The Astrophysical Journal Supplement Series, 268:32 (17pp), 2023 September https://doi.org/10.3847/1538-4365/ace1f5
© 2023. The Author(s). Published by the American Astronomical Society.
OPEN ACCESS

Powerful Radio Sources in the Southern Sky. II. A Swift X-Ray Perspective

F. Massaro[1,2,3,4], S. V. White[5], A. Paggi[6,7,8], A. Jimenez-Gallardo[1,2,9], J. P. Madrid[10], C. Mazzucchelli[11,12], W. R. Forman[13], A. Capetti[2], C. Leto[14], A. García-Pérez[1,15], C. C. Cheung[16], V. Chavushyan[13,15], N. P. H. Nesvadba[17], I. Andruchow[18,19], H. A. Peña-Herazo[20], E. Sani[11], R. Grossová[21,22], V. Reynaldi[19,23], R. P. Kraft[13], B. Balmaverde[7], and S. Cellone[19,24]

[1] Dipartimento di Fisica, Università degli Studi di Torino, via Pietro Giuria 1, I-10125 Torino, Italy; f.massaro@unito.it
[2] Istituto Nazionale di Astrofisica (INAF)—Osservatorio Astrofisico di Torino, via Osservatorio 20, I-10025 Pino Torinese, Italy
[3] Istituto Nazionale di Fisica Nucleare (INFN)—Sezione di Torino, via Pietro Giuria 1, I-10125 Torino, Italy
[4] Consorzio Interuniversitario per la Fisica Spaziale, via Pietro Giuria 1, I-10125 Torino, Italy
[5] Department of Physics and Electronics, Rhodes University, P.O. Box 94, Grahamstown 6140, South Africa
[6] Dipartimento di Fisica, Università degli Studi di Torino (UniTO), via Pietro Giuria 1, I-10125 Torino, Italy
[7] Istituto Nazionale di Astrofisica—Osservatorio Astrofisico di Torino, via Osservatorio 20, I-10025 Pino Torinese, Italy
[8] Istituto Nazionale di Fisica Nucleare—Sezione di Torino, via Pietro Giuria 1, I-10125 Torino, Italy
[9] Dipartimento di Fisica e Astronomia, Università di Bologna, via P. Gobetti 93/2, I-40129 Bologna, Italy
[10] Department of Physics and Astronomy, The University of Texas Rio Grande Valley, Brownsville, TX 78520, USA
[11] European Southern Observatory, Alonso de Córdova 3107, Vitacura, Región Metropolitana, Chile
[12] Instituto de Estudios Astrofísicos, Facultad de Ingeniería y Ciencias, Universidad Diego Portales, Avenida Ejercito Libertador 441, Santiago, Chile
[13] Center for Astrophysics, Harvard & Smithsonian, 60 Garden Street, Cambridge, MA 02138, USA
[14] ASI—Agenzia Spaziale Italiana, Via del Politecnico snc, I-00133 Roma, Italy
[15] Instituto Nacional de Astrofísica, Óptica y Electrónica, Luis Enrique Erro 1, Tonantzintla, Puebla 72840, México
[16] Space Science Division, Naval Research Laboratory, Washington, DC 20375, USA
[17] Université de la Côte d'Azur, Observatoire de la Côte d'Azur, CNRS, Laboratoire Lagrange, Bd de l'Observatoire, CS 34229, F-06304 Nice cedex 4, France
[18] Instituto Argentino de Radioastronomía, CONICET-CICPBA-UNLP, CC5 (1897) Villa Elisa, Prov. de Buenos Aires, Argentina
[19] Facultad de Ciencias Astronómicas y Geofísicas, Universidad Nacional de La Plata, Paseo del Bosque, B1900FWA La Plata, Argentina
[20] East Asian Observatory, 660 N. A'ohōkū Place, Hilo, HI 96720, USA
[21] Department of Theoretical Physics and Astrophysics, Faculty of Science, Masaryk University, Kotlářská 2, Brno CZ-611 37, Czech Republic
[22] Astronomical Institute of the Czech Academy of Sciences, Bocní II 1401, 141 00 Prague, Czech Republic
[23] Instituto de Astrofísica de La Plata (CCT La Plata-CONICET-UNLP), La Plata, Argentina
[24] Complejo Astronómico El Leoncito (CASLEO), CONICET-UNLP-UNC-UNSJ, Av. España 1512 (sur), J5402DSP San Juan, Argentina
Received 2023 January 21; revised 2023 May 13; accepted 2023 May 31; published 2023 September 7

Abstract

We recently constructed the G4Jy-3CRE, a catalog of extragalactic radio sources based on the GLEAM 4-Jy (G4Jy) sample, with the aim of increasing the number of powerful radio galaxies and quasars with similar selection criteria to those of the revised release of the Third Cambridge Catalog (3CR). The G4Jy-3CRE consists of a total of 264 radio sources mainly visible from the Southern Hemisphere. Here, we present an initial X-ray analysis of 89 G4Jy-3CRE radio sources with archival X-ray observations from the Neil Gehrels Swift Observatory. We reduced a total of 624 Swift observations, for about 0.9 Ms of integrated exposure time. We found X-ray counterparts for 59 radio sources belonging to the G4Jy-3CRE, nine of them showing extended X-ray emission. The remaining 30 sources do not show any X-ray emission associated with their radio cores. Our analysis demonstrates that X-ray snapshot observations, even if lacking uniform exposure times, as those carried out with Swift, allow us to (i) verify and/or refine the host galaxy identification; (ii) discover the extended X-ray emission around radio galaxies of the intracluster medium when harbored in galaxy clusters, as the case of G4Jy 1518 and G4Jy 1664; and (iii) detect X-ray radiation arising from their radio lobes, as for G4Jy 1863.

Unified Astronomy Thesaurus concepts: Radio active galactic nuclei (2134); Radio jets (1347); Radio lobes (1348); Radio loud quasars (1349); Galaxy clusters (584); Galactic and extragalactic astronomy (563); X-ray surveys (1824); Surveys (1671)

Supporting material: figure set, machine-readable table

1. Introduction

The Third Cambridge Catalog (3C; Edge et al. 1959) and its revised versions (3CR and 3CRR; Bennett 1962; Laing et al. 1983, respectively) is widely considered the gold standard among catalogs of powerful radio sources. Since their releases, they have enabled core investigations into the nature of radio-loud active galactic nuclei (i.e., radio galaxies and quasars; Begelman et al. 1984; Urry 1995; Harvanek et al. 2001; Hardcastle & Croston 2020), their environments at all scales, and feedback processes occurring therein (McNamara & Nulsen 2007, 2012; Fabian 2012; Morganti 2017).

The 3C benefits from an extensive list of surveys, all carried out over six decades, searching for counterparts at all wavelengths from radio (Wills & Parker 1966; Law-Green et al. 1995; Hardcastle & Worrall 2000; Giovannini et al. 2005), to infrared (IR; Simpson et al. 1999; Baldi et al. 2010; Werner et al. 2012; Dicken et al. 2014), optical (Djorgovski et al. 1988; Hiltner & Roeser 1991; Longair et al. 1995; McCarthy et al. 1995, 1996, 1997; de Koff et al. 1996;

Original content from this work may be used under the terms of the Creative Commons Attribution 4.0 licence. Any further distribution of this work must maintain attribution to the author(s) and the title of the work, journal citation and DOI.

Lehnert et al. 1999; Martel et al. 1999; Chiaberge et al. 2000; Buttiglione et al. 2009, 2010, 2011), and X-ray energies (Evans et al. 2006; Hardcastle et al. 2006; Balmaverde et al. 2012; Wilkes et al. 2013; Kuraszkiewicz et al. 2021). Many results were also achieved via follow-up observations performed at all frequencies as those obtained by (i) the Hubble Space Telescope (HST) snapshot survey of 3CR radio source counterparts[25] (Madrid et al. 2006; Privon et al. 2008; Chiaberge et al. 2015; Hilbert et al. 2016); (ii) the 3CR Chandra snapshot survey (Massaro et al. 2010, 2012, 2013, 2018; Stuardi et al. 2018; Jimenez-Gallardo et al. 2020); and, more recently, (iii) the MUse RAdio Loud Emission line Snapshot survey (MURALES; Balmaverde et al. 2018, 2018, 2019, 2021, 2022).

However, despite its success, the 3C suffers from an artificial limitation since it is restricted to the Northern Hemisphere. About 2/3 of 3C sources are not visible from the Southern Hemisphere, thus having limited access to modern astronomical facilities and instruments, such as the Multi Unit Spectroscopic Explorer (MUSE; Bacon et al. 2010) and the Enhanced Resolution Imager and Spectrograph (ERIS; Kenworthy et al. 2018) mounted at the Very Large Telescope (VLT), the Atacama Large Millimeter/submillimeter Array (ALMA), the MeerKAT radio telescope (see, e.g., Sejake et al. 2023), and the High Energy Stereoscopic System (HESS) at very high energies. In the near future, new facilities located in the Southern Hemisphere will include the Square Kilometre Array (SKA; McMullin et al. 2020), the Vera Rubin Observatory (a.k.a., Large Synoptic Survey Telescope—LSST; Ivezić et al. 2019), the Extremely Large Telescope[26] (ELT), and the Cherenkov Telescope Array (CTA).

Several attempts were made to create the southern equivalent of the 3C. For instance, Best et al. (1999) used the Molonglo Reference Catalogue (MRC; Large et al. 1981) to select an equatorial sample of 178 radio sources with flux density above 5 Jy at 408 MHz, in the range of decl. between $-30°$ and $10°$ and having Galactic latitudes $|b| \geqslant 10°$. This sample is characterized by a high spectroscopic completeness and its footprint mitigates the 3C observability limitation. Burgess & Hunstead (2006a, 2006b) created the Molonglo Southern 4-Jy (MS4) sample, a sample of southern radio sources at 408 MHz with integrated flux densities $S_{408} > 4.0$ Jy. However it was only until the Murchison Widefield Array (MWA; Tingay et al. 2013) became operational in Western Australia that the southern counterpart of the 3C at ∼178 MHz was finally created. We recently built a sample of 264 extragalactic radio sources extracted from the GaLactic and Extragalactic All-sky MWA 4-Jy (G4Jy) catalog (White et al. 2020a, 2020b), namely: the G4Jy-3CRE (Massaro et al. 2023, hereinafter Paper I), that is the southern equivalent to the 3CR in terms of its nominal flux limit threshold of 9 Jy (Bennett 1962; Spinrad et al. 1985).

In Paper I, we carried out a comparison between archival radio maps and optical images to search for G4Jy-3CRE host galaxies. This analysis was combined with an extensive literature search performed to identify those radio sources with a redshift, z, measurement. We found that 79% of the G4Jy-3CRE sources (i.e., 208 out of 264) have a clear optical counterpart to their radio cores. For 181 radio sources, the optical counterpart is also coincident with the mid-IR one reported in the G4Jy catalog (White et al. 2020a, 2020b). Using both the NASA Extragalactic Database (NED)[27] and the SIMBAD Astronomical Database,[28] we found spectroscopic z measurements for a total of 145 sources (out of 264), corresponding to ∼55% of the G4Jy-3CRE catalog. To be considered for this work, redshifts must have (i) a published figure of the optical spectrum or (ii) a description of such spectrum with emission and/or absorption lines clearly reported in a table and/or in the publication. These conservative criteria were already adopted in previous analyses and spectroscopic campaigns (see, e.g., Massaro et al. 2016; Peña-Herazo et al. 2020, 2022; Kosiba et al. 2023).

In this second paper of the series, we present a first X-ray perspective of the G4Jy-3CRE catalog based on targeted X-ray observations. By searching the archive of the X-Ray Telescope (XRT; Burrows et al. 2000, 2005) on board the Neil Gehrels Swift Observatory (Gehrels et al. 2004), we found that a total of 90 G4Jy-3CRE radio sources, out of 264, were already observed, with at least one observation having a nominal exposure time, $T_{\rm exp}$, above 250 s. The main aims of the current X-ray analysis are to (i) use the position of X-ray counterparts, when detected, to verify and eventually refine the results of the previous optical analysis (see Paper I for more details); (ii) test which sources show extended X-ray emission that could be a signature of emission from the intracluster medium (ICM) for those harbored in galaxy clusters and groups, and (iii) obtain measurements of their X-ray count rate, useful to plan X-ray follow-up observations.

We also compared Swift X-ray images with radio maps at different frequencies. Similar to Paper I, we mainly used those radio maps available in the databases of the Very Large Array (VLA) Low-Frequency Sky Survey Redux[29] (VLSSr; Cohen et al. 2007), the Tata Institute of Fundamental Research (TIFR) Giant Metrewave Radio Telescope (GMRT) Sky Survey (TGSS; Intema et al. 2017), the Sydney University Molonglo Sky Survey (SUMSS; Mauch et al. 2003), the National Radio Astronomy Observatory (NRAO) VLA Sky Survey (NVSS; Condon et al. 1998), and the VLA Sky Survey (VLASS; Lacy et al. 2020), corresponding to nominal frequencies of 74 MHz, 150 MHz, 843 MHz, 1.4 GHz, and 3 GHz, respectively, and the NRAO VLA Archive Survey (NVAS)[30] databases. This analysis is only devoted to X-ray observations and it does not include any optical and ultraviolet investigation feasible thanks to the observations collected with the Ultra-violet Optical Telescope (UVOT) instrument (Roming et al. 2005) on board Swift. A dedicated paper on broadband photometry for the G4Jy-3CRE sample, that includes also UVOT data, is currently in preparation (A. García-Pérez et al. 2023, in preparation).

This paper is structured as follows: Section 2 is dedicated to a brief overview of the G4Jy-3CRE catalog and the selection criteria underlying the Swift-XRT archival search. Section 3 is devoted to a description of the data reduction and analysis procedures adopted here while Section 4 is dedicated to the results we achieved. A comparison with previous X-ray analyses is also presented in Section 5 while Section 6 illustrates the search for mid-IR and optical counterparts using

[25] https://archive.stsci.edu/prepds/3cr/
[26] https://elt.eso.org
[27] http://ned.ipac.caltech.edu
[28] http://simbad.u-strasbg.fr/simbad/
[29] http://cade.irap.omp.eu/dokuwiki/doku.php?id=vlssr
[30] http://www.vla.nrao.edu/astro/nvas/

X-ray images. Summary, conclusions, and future perspectives are given in Section 7. Finally, the Appendix reports all Swift X-ray images with radio contours overlaid, including a comparison between Chandra and Swift X-ray observations for four sources having unpublished Chandra data sets.

As in Paper I, we adopt cgs units for numerical results and we assume a flat cosmology with $H_0 = 69.6$ km s^{-1} Mpc^{-1}, $\Omega_M = 0.286$, and $\Omega_\Lambda = 0.714$ (Bennett et al. 2014). Spectral indices, α, are defined by flux density, $S_\nu \propto \nu^{-\alpha}$. For optical images, we used those available in the archives of the Panoramic Survey Telescope & Rapid Response System (Pan-STARRS; Flewelling et al. 2020) and the Dark Energy Survey (DES; Abbott et al. 2018). These optical data were complemented by images available in the red filter of the Digital Sky Survey[31] (DSS), for those sources outside the Pan-STARRS and DES footprints. Pan-STARRS magnitudes are reported in the AB system (Oke 1974; Oke & Gunn 1983) while DES magnitudes are given in optical filters similar to those of Pan-STARRS and the Sloan Digital Sky Survey (SDSS; Ahn et al. 2012).

2. Sample Selection

The G4Jy-3CRE sample contains a total of 264 extragalactic radio sources (Paper I). The parent sample of the G4Jy-3CRE catalog was the larger complete sample of extragalactic radio sources with flux densities above the threshold of 4 Jy at 151 MHz, namely the G4Jy catalog (White et al. 2020a, 2020b) based on the recent GaLactic and Extragalactic All-sky MWA survey[32] (GLEAM; Wayth et al. 2015; Hurley-Walker et al. 2017). It is worth noting that MWA is considered as the SKA precursor at low radio frequencies (Tingay et al. 2013).

All radio sources included in the G4Jy-3CRE catalog lie at decl. $< -5°$, also having Galactic latitudes $|b| > 10°$, and are located outside the original footprint of the 3CR catalog. G4Jy-3CRE sources have flux density measurements at 174 MHz, S_{174} and at 181 MHz, S_{181}, integrated in the GLEAM subbands, above 8.13 Jy and 7.85 Jy, respectively, where these thresholds correspond to the 9 Jy limiting sensitivity, at ∼178 MHz, which is the nominal value adopted to create the 3CR. The flux density thresholds were computed assuming a power-law radio spectrum and adopting the spectral indices reported in the G4Jy catalog. Thus the G4Jy-3CRE is equivalent, in terms of radio flux density selection, to the northern 3CR extragalactic sample (Bennett 1962; Spinrad et al. 1985). We highlight that relatively bright sources at decl. $< +30°$ and Galactic latitudes $|b| > 10°$, including the Orion Nebula, were all masked in the GLEAM extragalactic catalog and are not listed in the G4Jy sample (see White et al. 2020a, 2020b, and references therein for a list of masked sources and additional details).

Here, we cross-matched the G4Jy-3CRE catalog with the Swift archive, adopting a search radius of 10′, and then we selected only sources having at least one XRT observation with nominal T_{exp} longer than 250 s. Our search was restricted only to X-ray observations performed in PHOTON COUNTING mode (Hill et al. 2004) to ensure that an X-ray image can be obtained and compared with those at other frequencies. Adopting these criteria, we found a total of 90 radio sources with Swift-XRT data available in the archive. We excluded G4Jy 1038 (aka 3C 279), one of the most famous blazars (see, e.g., Lynds et al. 1965; Stocke et al. 1998) because its Swift-XRT observations are already extensively discussed in the literature (see, e.g., Collmar et al. 2010; Hayashida et al. 2015; Larionov et al. 2020).

[31] https://archive.eso.org/dss/dss
[32] https://www.mwatelescope.org/gleam

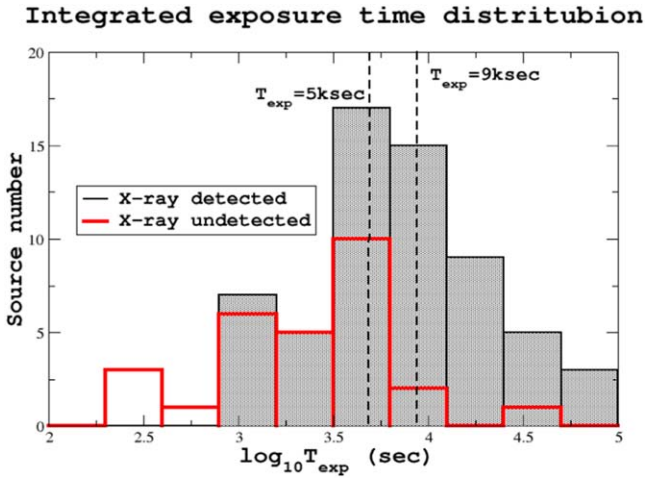

Figure 1. Integrated exposure times T_{exp} for all merged event files reduced in our analysis. The black histogram refers to radio sources having an X-ray-detected counterpart while the red one represents those for which no X-ray source is spatially coincident with the radio core. A total of 624 observations were retrieved from the Swift-XRT archive and analyzed to investigate the X-ray emission of 89 G4Jy-3CRE radio sources. The two dashed vertical lines mark the thresholds of 5 ks and 12 ks, respectively. We found an X-ray counterpart for all radio sources with integrated T_{exp} larger than ∼12 ks and for 85% of the sample (i.e., 35 out of 41) observed for more than 5 ks.

We processed a total of 624 individual observations for 89 radio sources belonging to the G4Jy-3CRE catalog. All these observations were acquired between 2005 May and 2022 December. Given that G4Jy 1748 and G4Jy 1749 lie in the same Swift-XRT field, with an ∼4′ angular separation, we processed only the nine archival observations centered on the former radio source.

The distribution of the integrated T_{exp} for the 89 radio sources is shown in Figure 1. We remark that even when the integrated T_{exp} appears relatively large (i.e., above ∼10 ks), it is the result of merging several, relatively short observations. Since the integrated T_{exp} for a large fraction of the sources (i.e., ∼90%) is smaller than ∼25 ks, this prevents us from performing a uniform spectral analysis. Thus, we focused on searching for X-ray counterparts and refining the mid-IR and optical analyses.

During our archival search, we also found four radio sources, namely, G4Jy 171, G4Jy 260, G4Jy 411, and G4Jy 1613 with unpublished Chandra X-ray observations. In these cases, we also reduced these Chandra data and we compared them with the results obtained from the Swift-XRT images. A brief overview of the Chandra data reduction procedure adopted here, together with a comparison between X-ray images collected by the two satellites, is reported in the Appendix.

3. Swift X-Ray Data Reduction and Analysis

3.1. X-Ray Source Detection

We adopted the same data reduction procedures described in previous Swift-XRT analyses (see, e.g., Massaro et al. 2008a, 2008b; Paggi et al. 2013; Marchesini et al. 2019, 2020), providing results in agreement with those of the Swift-XRT X-Ray point source catalogs (D'Elia et al. 2013;

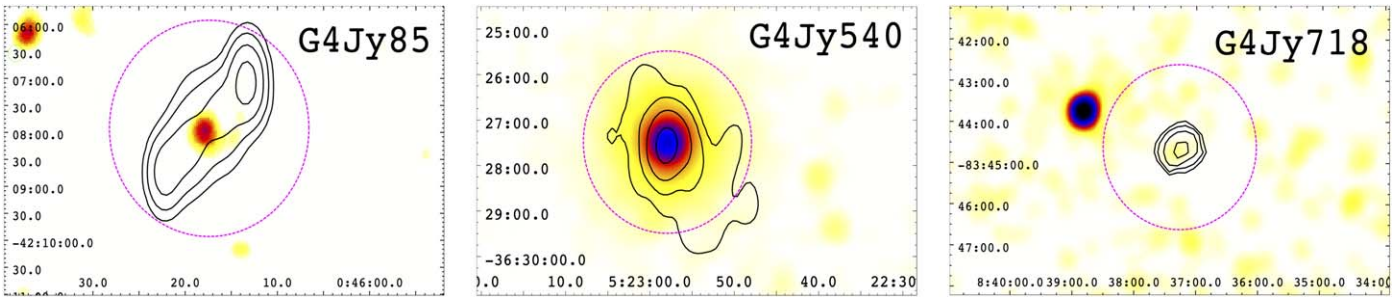

Figure 2. Left panel: the X-ray image, obtained from the merged event file of G4Jy 85, smoothed with a Gaussian kernel of 10 pixels (i.e., 23.″57). The magenta circle is centered on the position of the X-ray counterpart associated with this radio source and it has a radius of 120.″207 (i.e., 51 pixels) enclosing 90% of the Swift-XRT point-spread function (PSF). Radio contours are drawn using the radio map at 150 MHz starting at level of 0.3 Jy beam^{-1} and increasing by a factor of 3. This is a clear example of a radio source for which the X-ray counterpart of its radio core is detected at the level of the S/N reported in the figure. Center panel: same image as the left panel but for G4Jy 540, an example of detected extended X-ray emission. Here radio contours were computed using the archival radio map at 150 MHz starting at level of 0.1 Jy beam^{-1} and increasing by a factor of 6. Right panel: same image as the left panel but for G4Jy 718, an example of a radio source lacking an X-ray counterpart. In this case the magenta circle is centered on the radio position reported in the G4Jy catalog. Radio contours overlaid onto the X-ray image are drawn from the radio map at 843 MHz starting at level of 0.2 Jy beam^{-1} and increasing by a factor of 2.

(The complete figure set (90 images) is available.)

Evans et al. 2014, 2020). Therefore, we report here only basic details about the data reduction while additional information can be obtained from the references previously listed. The entire X-ray analysis performed here and all X-ray images shown in the following sections are restricted to the 0.5–10 keV energy range, unless stated otherwise.

Raw Swift-XRT data were downloaded from the archive[33] and reduced to obtain clean event files using the XRTPIPELINE task, which is part of the Swift X-Ray Telescope Data Analysis Software (XRTDAS; Capalbi et al. 2005), distributed within the HEAsoft package (version 6.30.1). Event files were calibrated and cleaned with standard filtering criteria using the XRTPIPELINE task, combined with the latest calibration files available in the High Energy Astrophysics Science Archive Research Center (HEASARC) calibration database (CALDB) version (v. 20220907).[34] In particular, using XSELECT, we excluded time intervals (i) with count rates higher than 40 photons per second and (ii) having the CCD temperature exceeding −50 °C in regions located at the edges of the XRT camera (D'Elia et al. 2013). Clean event files for the same sources were merged using the XSELECT task, while corresponding exposure maps were merged with the XIMAGE software.[35]

We created images for all merged event files and a detection run was then performed using the sliding cell DETECT (i.e., DET) algorithm in XIMAGE (Giommi et al. 1992). We chose a threshold of the signal-to-noise ratio (S/N) equal to 3 to claim an X-ray detection and we adopted the following X-ray detection flags (XDFs) to characterize the detection and the identification:

1. *x* (X-ray counterpart): all G4Jy-3CRE sources having a unique X-ray source located at the position of the radio source, within the X-ray positional uncertainty region, e.g., G4Jy 85 shown in left panel of Figure 2;
2. *e* (extended X-ray source): radio sources for which the X-ray counterpart, detected in the Swift-XRT image, shows diffuse/extended X-ray emission, e.g., G4Jy 540 in the central panel of Figure 2;
3. *u* (undetected X-ray counterpart): those merged event files for which the DET algorithm did not report an X-ray detection above the chosen threshold at the location of the radio source (see, e.g., G4Jy 718 in the right panel of Figure 2). We also used this flag for four sources for which their X-ray emission is contaminated by a nearby extended object, thus making it challenging to claim a detection (see the following sections for more details).

For all sources that are undetected in X-rays with the DET algorithm (labeled *u* in Table 1), we carried out a second detection run using the SOurce STAtistic (SOSTA) tool available in XIMAGE. The SOSTA algorithm uses a local background to determine the significance of a source detection and to estimate its count rate while detections performed using the DET procedure are based on the global background. Thus, the former algorithm could be more accurate for observations with relatively low integrated $T_{\rm exp}$. To perform this detection run we were prompted to select the radio source position to compute the background, source counts, count rate, and detection significance. Radio sources having a candidate X-ray counterpart detected using SOSTA have all an S/N below 3, computed using the DET task, and all the numbers of photons are reported without uncertainties in Table 1 to indicate that they correspond to a 3σ upper limit. The SOSTA algorithm does not provide the X-ray source position and thus it is not reported in Table 1.

In all merged event files, where we detected an X-ray counterpart to a G4Jy-3CRE radio source, we measured (i) the coordinates of the X-ray centroid (J2000 equinox) using the XRTCENTROID task, when detected using the DET algorithm; (ii) the number of photons n_{90}, within a circular region of radius equal to 120.″207 (i.e., 51 pixels) centered on the X-ray coordinates enclosing 90% of the Swift-XRT PSF; (iii) the expected number of background photons for the same area $n_{b,90}$; and (iii) the count rate, in photons s^{-1}, and the S/N of the X-ray detection when obtained with the DET algorithm. If no statistical uncertainty is reported on the measured count rate, this corresponds to a 3σ upper limit obtained with the SOSTA algorithm. All these parameters, together with the total number

[33] https://heasarc.gsfc.nasa.gov/docs/archive.html
[34] https://heasarc.gsfc.nasa.gov/docs/heasarc/caldb/caldb_supported_missions.html
[35] https://heasarc.gsfc.nasa.gov/xanadu/ximage/ximage.html

Table 1
Results for All G4Jy-3CRE Sources with Archival Swift-XRT Observations

G4Jy name	R.A.[r] (J2000)	Decl.[r] (J2000)	R.A.[x] (J2000)	Decl.[x] (J2000)	$n_{90}(n_{b,90})$ (ph)	Ctr (10^{-2} ph s^{-1})	S/N	T_{exp} (s)	N_{obs}	XDF	z	$N_{H,Gal}$ (1×10^{20} cm^{-2})
20	00:10:30.55	−44:22:57.00	⋯	⋯	24(20)	0.2(–)	⋯	5932	6	u	⋯	1.12
27	00:16:02.68	−63:10:07.21	⋯	⋯	25(36)	0.1(0.05)	1.8	4072	6	u	⋯	1.52
77	00:41:29.21	−09:22:40.01	⋯	⋯	0(109)	⋯	⋯	6722	6	u	⋯	2.69
78	00:42:09.19	−44:14:01.68	00:42:08.5	−44:13:57.2	47(58)	0.48(0.11)	4.2	6038	6	x	0.346 (a)	2.61
85	00:46:16.85	−42:07:42.89	00:46:17.4	−42:07:55.7	103(26)	1.04(0.14)	7.4	7128	5	x	0.0526 (b)	1.13
86	00:47:33.66	−25:17:07.37	00:47:33.2	−25:17:32.8	4474(118)	13.5(0.23)	59.6	32,008	13	e	0.00081 (c)	2.79
93	00:52:14.88	−43:06:29.18	00:52:14.6	−43:06:27.3	44(30)	0.45(0.11)	4.1	5273	5	x	⋯	1.17
120	01:05:20.91	−45:05:28.00	⋯	⋯	14(10)	0.51(–)	⋯	2267	3	u	⋯	1.64
162	01:30:27.96	−26:09:58.86	⋯	⋯	2(5)	1.54(–)	⋯	995	1	u	2.34665 (d)	1.31
168	01:31:36.53	−07:03:57.20	⋯	⋯	2(4)	2.46(–)	⋯	1033	1	u	⋯	3.5
171	01:34:00.69	−36:29:01.79	01:33:57.5	−36:29:37.1	165(39)	0.86(0.1)	8.7	11,744	2	x	0.02977 (e)	1.72
213	02:00:12.15	−30:53:26.48	02:00:12.3	−30:53:28.7	31(4)	2.93(0.57)	5.1	1221	1	x	0.6768 (f)	1.54
217	02:02:14.04	−76:20:06.29	02:02:12.8	−76:19:56.7	124(12)	7.53(0.74)	10.1	1750	3	x	0.38939 (g)	5.51
247	02:19:02.81	−36:26:12.23	02:19:03.0	−36:26:05.7	50(16)	5.4(0.9)	6.0	930	1	x	0.488815 (h)	1.81
249	02:20:08.18	−70:22:27.80	02:20:08.2	−70:22:29.9	111(33)	2.56(0.28)	9.1	4606	8	x	⋯	6.06
257	02:23:57.55	−70:59:46.55	⋯	⋯	12(72)	0.4(–)	⋯	3603	5	u	⋯	6.17
260	02:25:02.61	−23:12:47.59	02:25:02.8	−23:12:47.7	111(77)	13.4(0.31)	43.7	20,139	7	x	0.232241 (d)	1.59
290	02:43:44.50	−51:12:33.59	⋯	⋯	1(1)	0.57(–)	⋯	311	1	u	⋯	2.0
293	02:46:56.26	−55:41:22.74	⋯	⋯	17(39)	0.28(–)	⋯	4315	7	u	⋯	2.59
304	02:52:46.31	−71:04:36.19	⋯	⋯	17(19)	0.1(0.06)	1.6	2888	2	u	0.56288 (a)	4.24
373	03:38:46.45	−35:22:46.26	⋯	⋯	0(202)	0.0(–)	⋯	34,042	15	u	0.1126 (i)	1.42
392	03:52:31.88	−07:11:04.03	03:52:30.6	−07:11:05.2	93(43)	0.95(0.14)	6.9	6599	5	x	0.96354 (j)	4.87
404	04:00:16.51	−16:10:13.58	⋯	⋯	12(3)	2.34(–)	1.4	1033	1	u	0.584 (d)	1.97
411	04:05:33.94	−13:08:14.39	04:05:34.1	−13:08:12.3	3510(134)	9.68(0.19)	50.0	37,306	15	x	0.57055 (j)	4.11
415	04:07:48.44	−12:11:33.40	04:07:48.4	−12:11:34.0	1375(23)	34.4(1.0)	33.4	4398	4	x	0.5731 (k)	3.54
416	04:08:20.25	−65:45:10.66	⋯	⋯	35(11)	0.68(–)	⋯	1996	1	u	0.962 (l)	3.68
427	04:12:48.02	−56:00:48.82	⋯	⋯	33(37)	0.29(–)	⋯	4448	3	u	⋯	0.9
446	04:20:56.43	−62:23:36.94	⋯	⋯	15(49)	0.13(0.08)	1.7	4002	5	u	⋯	1.82
464	04:29:40.22	−36:30:56.02	04:29:40.0	−36:30:50.7	58(16)	0.99(0.21)	4.8	3678	2	x	⋯	1.34
492	04:44:37.45	−28:09:48.33	04:44:37.6	−28:09:53.7	1661(70)	11.5(0.3)	38.9	15,533	3	x	0.147 (a)	2.46
506	04:55:14.31	−30:06:47.20	04:55:13.9	−30:06:50.4	38(23)	0.41(0.12)	3.4	4533	2	x	⋯	1.06
510	04:56:09.84	−21:59:15.98	04:56:08.9	−21:59:11.5	489(18)	10.8(0.51)	21.0	4982	1	x	0.533 (m)	2.77
518	05:06:43.75	−61:09:41.51	05:06:43.8	−61:09:41.1	45,86(771)	4.97(0.09)	53.6	96,348	82	x	1.093 (n)	1.95
540	05:22:57.90	−36:27:29.67	05:22:57.9	−36:27:29.3	44,910(376)	56.6(0.27)	210.9	88,761	50	e	0.056546 (o)	3.24
563	05:36:13.67	−49:44:23.10	05:36:13.9	−49:44:20.3	35(30)	0.48(0.11)	4.2	5120	6	x	⋯	3.01
580	05:49:23.49	−40:51:13.04	⋯	⋯	43(47)	0.11(0.06)	2.0	7479	7	u	⋯	3.57
613	06:26:47.21	−54:32:46.20	06:26:49.8	−54:32:35.9	447(41)	0.54(0.11)	4.9	6629	2	e	0.051976 (p)	7.83
614	06:27:06.94	−35:29:12.93	06:27:06.7	−35:29:16.2	7613(578)	24.7(0.33)	73.9	33736	14	x	0.054855 (q)	6.32
618	06:35:45.05	−75:16:15.31	06:35:46.3	−75:16:15.8	9052(282)	16.7(0.21)	80.5	62,843	67	x	0.653 (r)	7.23
619	06:36:31.30	−20:34:38.00	06:36:32.2	−20:34:53.5	194(193)	0.34(0.05)	7.5	25,274	10	x	0.055198 (s)	20.6
644	07:09:21.90	−36:02:10.26	07:09:14.2	−36:01:22.6	1260(53)	6.83(0.23)	29.5	20,319	5	x	0.11 (t)	16.3
651	07:17:06.38	−36:21:52.95	07:17:08.9	−36:22:08.0	156(21)	0.98(0.26)	3.8	2061	2	e	0.031358 (h)	19.1
672	07:43:32.63	−67:26:28.61	07:43:31.8	−67:26:24.4	199(9)	8.61(0.68)	12.7	2868	2	x	1.512 (u)	8.95
718	08:37:14.08	−83:44:40.49	⋯	⋯	42(25)	0.33(–)	⋯	4473	4	u	⋯	10.8
721	08:39:50.80	−12:14:26.56	08:39:50.5	−12:14:34.4	8752(69)	33.4(0.42)	79.3	27,184	7	x	0.19787 (v)	5.43
723	08:41:26.19	−75:40:31.12	08:41:26.6	−75:40:25.6	101(17)	7.18(0.77)	9.4	1414	1	x	0.521 (w)	7.52
835	10:18:09.23	−31:44:15.50	10:18:08.9	−31:44:12.8	70(22)	1.68(0.24)	7.0	3786	3	x	1.346 (x)	5.1
836	10:19:43.84	−42:24:50.34	⋯	⋯	26(37)	0.37(–)	1.2	5403	7	u	⋯	7.91
854	10:33:13.07	−34:18:43.99	⋯	⋯	20(14)	0.67(–)	1.6	3360	5	u	⋯	5.5
876	10:51:30.35	−09:18:13.19	10:51:29.7	−09:18:09.3	1028(53)	11.5(0.38)	30.5	9523	10	x	0.345296 (k)	2.96
917	11:25:54.63	−35:23:22.66	⋯	⋯	11(4)	4.04(–)	0.8	451	1	u	0.033753 (y)	5.97
927	11:34:23.58	−17:27:51.70	11:34:23.8	−17:27:49.4	137(73)	0.59(0.08)	7.2	14,221	14	x	1.618 (d)	2.82
933	11:39:10.69	−13:50:42.90	11:39:10.5	−13:50:40.9	530(34)	7.11(0.36)	20.0	8066	1	x	0.556458 (a)	3.27
950	11:45:30.94	−48:36:10.40	11:45:30.9	−48:36:10.9	161(46)	2.9(0.3)	9.8	5203	7	x	⋯	10.4
1034	12:54:37.02	−12:33:29.47	12:54:35.4	−12:34:00.6	24(13)	1.21(0.4)	3.0	990	3	x	0.015464 (z)	3.07
1071	13:30:07.18	−21:42:04.50	13:30:07.0	−21:41:56.9	63(4)	5.58(0.77)	7.2	1279	3	x	0.528 (α)	7.1

Table 1
(Continued)

G4Jy name	R.A.[r] (J2000)	Decl.[r] (J2000)	R.A.[x] (J2000)	Decl.[x] (J2000)	$n_{90}(n_{b,90})$ (ph)	Ctr (10^{-2} ph s^{-1})	S/N	T_{exp} (s)	N_{obs}	XDF	z	$N_{H,Gal}$ (1×10^{20} cm^{-2})
1079	13:34:16.65	−10:09:23.54	13:34:18.6	−10:09:26.0	75(36)	0.26(0.08)	3.4	10,533	1	x	⋯	2.34
1080	13:36:38.91	−33:58:03.45	13:36:38.8	−33:57:57.6	294(78)	2.75(0.21)	12.8	7562	10	x	0.0125 (β)	3.96
1135	14:16:33.65	−36:40:47.02	14:16:33.1	−36:40:51.4	167(39)	2.05(0.19)	10.8	7108	5	x	0.0747 (γ)	4.0
1136	14:16:41.12	−21:46:18.01	14:16:40.8	−21:46:12.1	165(73)	0.37(0.05)	7.0	20,186	10	x	1.116 (δ)	7.74
1145	14:19:49.70	−19:28:32.22	14:19:49.6	−19:28:22.9	1500(40)	17.4(0.52)	33.8	8934	3	x	0.1195 (ϵ)	7.19
1148	14:20:04.09	−49:35:47.49	14:20:03.0	−49:35:40.3	360(31)	1.91(0.26)	7.5	4285	3	e	0.09142 (γ)	13.9
1158	14:24:31.90	−49:13:48.13	14:24:31.9	−49:13:54.5	65(35)	0.77(0.16)	4.8	4977	8	x	0.662 (ζ)	14.5
1192	14:48:29.05	−47:01:39.90	14:48:28.3	−47:01:45.3	33(18)	0.41(0.14)	3.1	3600	4	x	⋯	9.33
1203	14:54:28.53	−36:39:57.32	⋯	⋯	86(74)	0.3(–)	1.7	8808	9	u	⋯	5.31
1225	15:10:53.55	−05:43:07.10	15:10:53.4	−05:43:07.4	314(108)	1.87(0.13)	14.4	16,150	7	x	1.191 (η)	5.96
1279	15:48:59.13	−32:17:04.14	⋯	⋯	51(29)	0.51(–)	0.5	2896	1	u	0.1082 (γ)	6.9
1411	17:25:26.13	−80:04:46.04	⋯	⋯	3.0(3)	1.66(–)	⋯	817	2	u	⋯	6.25
1423	17:37:37.14	−56:33:50.71	17:37:35.7	−56:34:04.3	80(64)	2.82(0.38)	7.5	2482	4	x	0.09846 (a)	6.64
1432	17:42:01.59	−60:55:22.39	17:42:01.2	−60:55:12.6	1707(96)	18.1(0.52)	35.0	10,350	5	x	⋯	6.2
1472	18:19:34.76	−63:45:48.27	18:19:34.7	−63:45:47.7	312(34)	4.99(0.33)	15.3	6070	7	x	0.06412 (θ)	6.06
1477	18:22:16.23	−63:59:16.76	18:22:16.3	−63:59:17.1	27(16)	1.58(0.37)	4.2	1542	2	x	⋯	6.79
1498	18:37:42.05	−43:35:32.77	⋯	⋯	5.0(2)	5.55(–)	⋯	263	1	u	⋯	6.5
1518	19:15:47.88	−26:52:57.84	19:15:48.8	−26:52:51.9	189(37)	1.3(0.21)	6.0	4017	6	e	0.226 (d)	7.66
1605	20:10:28.97	−56:26:28.75	⋯	⋯	0.0(11)	⋯	⋯	837	2	u	⋯	4.48
1613	20:18:05.16	−55:40:28.39	20:18:01.0	−55:39:29.0	392(64)	1.85(0.12)	15.5	17,280	4	x	0.060629 (y)	4.77
1635	20:33:16.60	−22:53:20.90	20:33:16.6	−22:53:17.0	594(39)	7.43(0.35)	21.0	8939	4	x	0.131491 (r)	4.01
1640	20:35:47.60	−34:54:02.67	⋯	⋯	6.0(25)	1.46(–)	⋯	827	2	u	⋯	2.58
1664	20:56:04.34	−19:56:35.41	20:56:04.2	−19:56:30.6	88(19)	1.39(0.31)	4.5	1968	8	e	0.15662 (λ)	5.09
1671	21:01:38.97	−28:01:45.58	⋯	⋯	33(13)	0.52(0.29)	1.8	1346	2	u	0.039444 (y)	7.31
1708	21:37:44.45	−14:32:54.22	21:37:45.3	−14:32:53.9	2251(98)	20.7(0.51)	40.9	12,461	17	x	0.20047 (μ)	4.15
1717	21:43:33.18	−43:12:47.79	21:43:33.2	−43:12:46.1	77(26)	1.03(0.19)	5.5	4363	8	x	⋯	1.48
1723	21:47:23.97	−81:32:07.79	⋯	⋯	2.0(4)	3.46(–)	⋯	333	1	u	⋯	8.3
1748	21:57:06.78	−69:41:21.66	21:57:05.8	−69:41:22.0	5176(99)	32.4(0.46)	70.4	18,150	9	e	0.0281 (ν)	2.49
1749	21:57:47.60	−69:41:53.59	21:57:48.3	−69:41:53.3	264(99)	0.41(0.06)	6.9	18,150	9	x	⋯	2.5
1757	22:06:10.33	−18:35:39.01	⋯	⋯	23(18)	0.67(–)	1.3	3641	4	u	0.6185 (ξ)	2.3
1822	23:21:02.01	−16:23:05.21	23:21:01.8	−16:23:03.6	33(21)	0.61(0.15)	4.0	3337	2	x	1.414 (d)	1.69
1840	23:34:26.63	−41:25:26.02	⋯	⋯	8.0(12)	1.26(–)	1.3	1700	4	u	0.907 (x)	1.5
1863	23:59:03.71	−60:55:13.55	23:59:04.1	−60:54:59.8	236(31)	2.39(0.22)	11.0	7118	1	e	0.0959 (y)	1.4

Note. Column (1): the G4Jy name of the radio source, also adopted in the G4Jy-3CRE catalog; columns (2, 3): the R.A. and the decl. (Equinox J2000) of the brightness-weighted radio centroid as reported in the G4Jy catalog, respectively; columns (4, 5): the R.A. and the decl. (Equinox J2000) measured from the distribution of the X-ray photons for radio sources with XDF = *x* or XDF = *e*, respectively; column (6): the number of photons measured in the 0.5–10 keV energy range within a circular region enclosing 90% of the Swift-XRT PSF, together with the average number of photons expected in the background for the same area, as reported in parenthesis; column (7): the X-ray count rate measured in photons s^{-1} with the 1σ uncertainty in parenthesis as obtained using the DET algorithm. For those sources having not statistical uncertainties reported, thus indicated with a dashed line, the count rate corresponds to a 3σ upper limit obtained using the SOSTA algorithm; column (8): the value of the S/N for all radio sources with an X-ray counterpart detected using the DET algorithm. X-ray counterparts, at S/N < 3 correspond to those detected when running the SOSTA algorithm and in these cases no X-ray coordinates were computed; column (9): the integrated T_{exp}; col. (10): the total number of sources reduced and analyzed; column (11): the XDF assigned in our analysis ("*x*" labels radio sources with a detected X-ray point-like counterpart, "*e*" stands for radio sources with extended X-ray emission around their radio cores, and "*u*" for G4Jy-3CRE with radio cores undetected in the X-ray band); column (12): the redshift z obtained from the literature analysis presented in Paper I, a question mark indicates sources with uncertain z estimates; and column (13): the Galactic column density $N_{H,Gal}$ (HI4PI Collaboration et al. 2016).

References. (a) Tadhunter et al. (1993); (b) Whiteoak (1972); (c) Springob et al. (2005); (d) Best et al. (1999); (e) Burbidge & Burbidge (1972); (f) Jones et al. (2004); (g) Jauncey et al. (1978); (h) Jones et al. (2009); (i) Carter & Malin (1983); (j) Lynds (1967); (k) Kinman & Burbidge (1967); (l) Labiano et al. (2007); (m) Wright et al. (1979); (n) Wright et al. (1977); (o) Sbarufatti et al. (2006); (p) Cava et al. (2009); (q) Quintana & Ramirez (1995); (r) Hunstead et al. (1978); (s) Storchi-Bergmann et al. (1996); (t) Parisi et al. (2014); (u) Bergeron & Kunth (1984); (v) Ho & Kim (2009); (w) Browne & Savage 1977); (x) di Serego Alighieri et al. (1994); (y) Tritton (1972); (z) Borne & Hoessel (1984); (α) Burbidge & Kinman (1966); (β) Younis et al. (1985); (γ) Simpson et al. (1993); (δ) Best et al. (2000); (ϵ) Burbidge (1967); (ζ) Marshall et al. (2011); (η) Peterson & Bolton (1972); (θ) Thompson et al. (1990); (λ) Stickel & Kuehr (1994); (μ) Baldwin (1975); (ν) Marenbach & Appenzeller (1982); (ξ) Morton & Tritton (1982). (See also Paper I for more details.)

(This table is available in machine-readable form.)

of X-ray observations processed per source, the integrated $T_{\rm exp}$, and the value of the XDF, are reported in Table 1.

Finally, in the Appendix, we show X-ray images for all merged event files with radio contours overlaid and a magenta dashed circle of 120.″207 superimposed, as in Figure 2. The circular region is centered on either the location of the X-ray counterpart of each G4Jy-3CRE radio source, if detected by Swift-XRT, or on its radio coordinates, as reported in the G4Jy catalog, if not. The frequencies of the radio maps used to draw the radio contours and the contour parameters are reported in the Appendix (see Table 2 for more details).

3.2. Extended X-Ray Emission

To determine whether an X-ray source is extended we adopted the following criterion. We assumed a Poissonian distribution for all measured numbers of photons and their uncertainties. We counted the difference δn between the number of photons (n_{10}) within an annulus of inner radius equal to 40.″069 (i.e., 17 pixels) and outer radius of 120.″207 (i.e., 51 pixels) and that of background photons $n_{b,10}$ expected in a region having the same area, $\delta n = n_{10} - n_{b,10}$. According to the latest model release of the PSF for Swift-XRT,[36] a circular region of 40.″069 and 120.″207 encloses 80% and 90% of the PSF, respectively. Thus, we expect that the measured number of photons δn, for a point-like source, corresponds to ∼10% of the total flux.

Consequently, we computed 10% of the total number of expected photons $n_{\rm ex}$ rescaling those (i.e., n_{90}) measured within a circular region of 120.″207 and subtracting the average background photons ($n_{b,90}$) expected for the same area, $n_{\rm ex} = \frac{1}{9}(n_{90} - n_{b,90})$. We considered as extended those X-ray sources for which the difference ($\delta n - n_{\rm ex}$) is larger than zero within a level of confidence of 3σ. The number of background photons was obtained by measuring counts within a circular region of 102 pixels in radius, masking other X-ray sources detected using the DET algorithm with an S/N > 3, in all merged event files, and then rescaled for the ratio of the areas. For extended X-ray sources, if the DET algorithm detected more than a single source close to the X-ray intensity peak, we only reported in Table 1 the one with the highest S/N.

4. Results

4.1. An X-Ray Overview of the Whole Sample

We found that all 25 G4Jy-3CRE sources with an integrated exposure time above $T_{\rm exp} \simeq 9$ ks have an X-ray counterpart. The only exception is G4Jy 373, an FR II radio galaxy at $z = 0.1126$ (Carter & Malin 1983) lying behind the Fornax Cluster at an angular separation of ∼5′ from NGC 1399 (see, e.g., Killeen et al. 1988; Hilker et al. 1999), for which the extended X-ray emission of the nearby galaxy cluster prevents us from detecting its X-ray counterpart. When selecting a threshold of integrated $T_{\rm exp}$ above 5 ks, 88% of sources (i.e., 36 out of 42) have an X-ray counterpart, as shown in Figure 1.

There are 30 radio sources with no X-ray emission associated with their radio cores, flagged as undetected. This list also includes G4Jy 77 and G4Jy 1605, which are two extended radio sources, where the former is a radio phoenix of the galaxy cluster A85 (see, e.g., Bagchi et al. 1998; Kempner et al. 2004; Ichinohe et al. 2015) while the latter is the radio

[36] https://heasarc.gsfc.nasa.gov/docs/heasarc/caldb/swift/docs/xrt/SWIFT-XRT-CALDB-10_v01.pdf

Table 2
Parameters of the Radio Contours Overlaid on the X-Ray Images

G4Jy Name	ν (MHz)	$l_{\rm min}$ (Jy beam^{-1})	Binning Factor
20	150	0.1	×4
27	843	0.3	×2
77	150	0.05	×2
78	150	0.3	×3
85	150	0.3	×3
93	150	0.3	×3
120	150	0.1	×3
162	150	0.1	×4
168	150	0.025	×4
171	150	0.05	×3
213	1400	0.4	×2
217	843	0.1	×3
247	150	0.1	×3
249	843	0.3	×2
257	843	0.2	×2
260	150	0.1	×4
290	150	1.6	×2
293	843	0.1	×2
843	843	0.3	×3
373	3000	0.002	×3
392	3000	0.01	×3
404	150	0.1	×4
411	150	0.1	×4
415	150	0.1	×4
416	843	1.6	×2
427	843	0.3	×3
446	843	0.6	×2
464	150	0.1	×4
492	3000	0.005	×2
506	3000	0.002	×2
510	150	0.1	×3
518	843	0.3	×2
540	150	0.1	×6
563	150	0.1	×4
580	150	0.1	×4
613	843	0.15	×2
614	150	0.1	×3
618	843	0.6	×2
619	150	0.1	×3
644	1400	0.005	×3
651	150	0.1	×2
672	843	0.1	×4
718	843	0.2	×2
721	150	0.1	×4
723	843	0.1	×3
835	150	0.1	×4
836	150	0.1	×4
854	150	0.1	×4
876	150	0.05	×4
917	3000	0.006	×2
927	150	0.1	×4
933	150	0.1	×4
950	150	0.1	×4
1034	3000	0.002	×2
1071	150	0.1	×4
1079	150	0.1	×4
1080	1400	0.04	×2
1135	150	0.1	×2
1136	150	0.1	×4
1145	150	0.2	×2
1148	150	0.2	×3
1158	150	0.1	×4
1192	150	0.1	×4
1203	1400	0.001	×4

Table 2
(Continued)

G4Jy Name	ν (MHz)	$l_{\rm min}$ (Jy beam^{-1})	Binning Factor
1225	150	0.1	×4
1279	150	0.02	×3
1411	843	0.2	×2
1423	843	0.1	×4
1432	843	0.16	×2
1472	843	0.16	×2
1477	843	0.1	×3
1498	150	0.1	×3
1518	150	0.02	×4
1605	843	0.01	×2
1613	843	0.01	×3
1635	3000	0.001	×3
1640	150	1.6	×2
1664	150	0.1	×3
1671	150	0.1	×2
1708	150	0.1	×4
1717	150	0.3	×3
1723	843	0.1	×3
1748	843	0.1	×4
1757	150	0.1	×4
1822	150	0.1	×4
1840	150	0.16	×2
1863	843	0.1	×3

Note. Column (1): the G4Jy name of the radio source, also adopted in the G4Jy-3CRE catalog; column (2): frequency of the radio map used to draw contours in units of MHz; column (3): minimum level of the radio contours $l_{\rm min}$; and column (4): binning factor for the radio contours.

relic of A3667 (see, e.g., Johnston-Hollitt et al. 2008; Owers et al. 2009). These sources are not expected to be associated with an X-ray point-like counterpart.

We also found nine radio sources with extended X-ray emission around them. However, for three out of the nine sources, namely G4Jy 416, G4Jy 651, and G4Jy 1749, their diffuse emission is contaminated by that of a nearby X-ray object. These sources are all marked as undetected. Signatures of extended X-ray emission are also evident in G4Jy 1863, the only source for which we claim the X-ray detection of its radio lobes, as described below. The remaining 50 radio sources have a detected X-ray point-like counterpart associated with their radio core.

Five out of the nine sources with extended X-ray emission are well known since their Chandra and XMM-Newton observations have been extensively discussed in the literature. These radio sources are (i) G4Jy 86 (aka the Sculptor Galaxy; see, e.g., Hoopes et al. 1996) a nearby star-forming galaxy at $z = 0.00081$ (Springob et al. 2005); (ii) G4Jy 540 (aka PKS 0521-36) a γ-ray emitting blazar (Abdollahi et al. 2020) with an X-ray jet detected by Chandra (see, e.g., Birkinshaw et al. 2002; Massaro et al. 2011); (iii) G4Jy 613, known to be associated with the galaxy cluster A3395 (Abell 1958; Abell et al. 1989; Quintana & Ramirez 1995; Ebeling et al. 1996; Sun 2009); (iv) G4Jy 1148 (aka PKS 1416-49), harbored in a non–cool core galaxy cluster detected by Chandra (Worrall & Birkinshaw 2017); and (v) G4Jy 1748 (aka PKS 2152-69), a lobe-dominated quasar hosted in a galaxy cluster with X-ray cavities inflated by radio plasma (Young et al. 2005) and hotspots detected in X-rays (see also Ly et al. 2005; Massaro et al. 2011).

Finally, we remark that adopting the same criteria described in Section 3 to determine the presence of diffuse X-ray emission, but using an earlier PSF model (Moretti et al. 2004) extensively adopted in the literature to search for galaxy clusters in Swift-XRT deep observations (see, e.g., Tundo et al. 2012; Liu et al. 2013; Tozzi et al. 2014; Dai et al. 2015; Liu et al. 2015), the following sources would be also identified as extended: G4Jy 260, G4Jy 411, G4Jy 415, G4Jy 492, G4Jy 614, G4Jy 618, G4Jy721, G4Jy 876, and G4Jy 1080. In particular, for some of these radio sources we found in the literature that G4Jy 415 is a quasar at $z = 0.5731$ that resides in a galaxy group (Johnson et al. 2018), and diffuse X-ray emission has been previously detected around G4Jy 492 (Mingo et al. 2017), G4Jy 721, an FR II radio galaxy harbored in a galaxy cluster (Yee & Green 1983; Ellingson et al. 1987, 1989; Yates et al. 1989), and G4Jy 876, which also lies in a galaxy-rich large-scale environment (Hintzen et al. 1983; Ellingson 1988; Ellingson et al. 1991; Hutchings et al. 1996). G4Jy 1080 is the brightest galaxy (aka IC 4296; see, e.g., Killeen et al. 1986; Wegner et al. 2003; Grossová et al. 2019; Condon et al. 2021; Grossová et al. 2022; and references therein) of the A3565 galaxy cluster (Abell 1958; Abell et al. 1989) at $z = 0.0125$ (see, e.g., Sandage 1978; Efstathiou et al. 1980) while G4Jy 614, a BL Lacertae object detected at TeV energies (aka PKS 0625-35), also belongs to the galaxy cluster A3392 (Abell 1958; Abell et al. 1989; Quintana & Ramirez 1995; Ebeling et al. 1996; Sun 2009).

4.2. Extended X-Ray Emission around G4Jy 1518 and G4Jy 1664

We found clear signatures of extended X-ray emission around two radio sources in the Swift-XRT images: G4Jy 1518 and G4Jy 1664.

G4Jy 1518 belongs to the equatorial sample of Best et al. (1999) and it is classified as a radio galaxy lying at $z = 0.226$. It is also listed in the MRC of radio sources (MRC 1912-269; Large et al. 1981). From a radio perspective, G4Jy 1518 appears to be a "restarted" radio galaxy, as shown in the archival radio maps of Figure 3. The host galaxy identification is consistent with detection of the radio core, as recently shown using MeerKAT observations (Sejake et al. 2023).

G4Jy 1664 is a radio galaxy at $z = 0.15662$ (aka 6dF J2056043-195635; Stickel & Kuehr 1994; Jones et al. 2009) with a classical FR II radio morphology, as shown in Figure 4. The redshift estimate was originally derived from stellar absorption features, clearly present in its optical spectrum. The radio core emission appears to be similar to giga-peaked radio sources (O'Dea et al. 1991).

4.3. X-Ray Counterparts of Radio Lobes in G4Jy 1863

An intriguing case is G4Jy 1863, a narrow-line hard X-ray-selected giant radio galaxy (Cusumano et al. 2010; Oh et al. 2018; Bruni et al. 2020) at $z = 0.0959$ (Tritton 1972; Danziger & Goss 1983; Ramos Almeida et al. 2011) lying in the direction of the galaxy cluster A4067 (Abell 1958; Abell et al. 1989; Teague et al. 1990) and shown in Figure 5. G4Jy 1863 shows several signatures of a past merger in its optical image, for instance it has several irregular shells and two faint arcs (Ramos Almeida et al. 2011).

In Figure 5 the red circles mark the positions of detected X-ray sources close to the radio structure of G4Jy 1863, and in

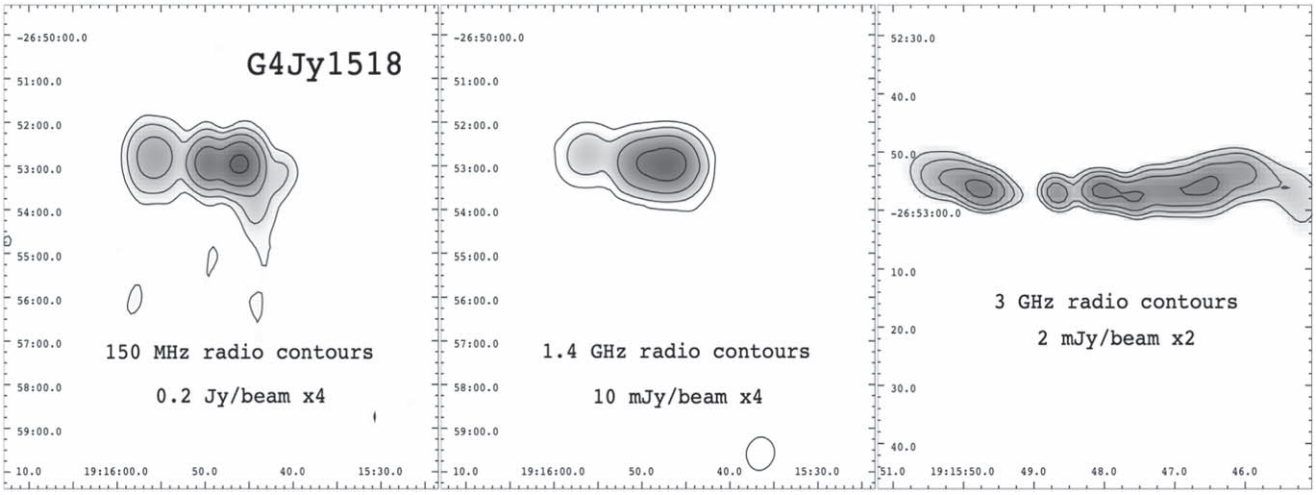

Figure 3. Radio maps for G4Jy 1518 retrieved from the TGSS, NVSS, and VLASS archives (left to right panels) at 150 MHz, 1.4 GHz, and 3 GHz, respectively. The frequency of the radio map from which contours were drawn is reported together with the intensity of the first level. All radio contours increase in level by a binning factor as indicated. The radio morphology of G4Jy 1518 shows a classical double-double radio structure similar to "restarted" radio galaxies.

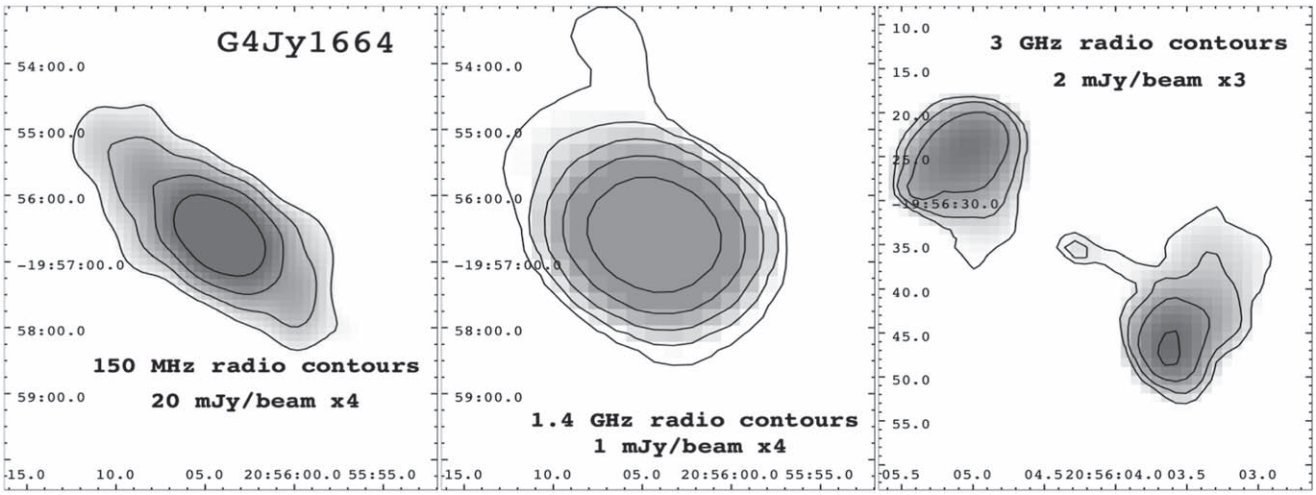

Figure 4. Same as Figure 3 but for G4Jy 1664. The radio morphology of G4Jy 1664 is typical of FR II radio sources at 3 GHz, while it appears a bit extended at lower frequencies where the double radio structure does not appear.

particular those labeled as S1 and S2. These two point-like sources have clear optical and mid-IR counterparts, as shown in the central and right panels of the same figure. The proximity of these two X-ray sources prevented us from claiming the presence of extended X-ray emission according to the procedure previously described.

However, considering the number of photons associated with both the northern and the southern radio lobes, in circular regions of 20 pixel radius, in comparison with those expected in the background for the same area, we claim a detection above a 3σ level of confidence for the X-ray counterparts of its radio lobes. This could be due to inverse Compton scattering off seed photons arising from the cosmic microwave background (see, e.g., Hoyle 1965; Longair 1970; Harris & Grindlay 1979; Hardcastle et al. 2002; Croston et al. 2005; Harris & Krawczynski 2006; Worrall 2009).

5. Comparison with Previous X-Ray Analyses

The results obtained with our detection analysis are in agreement with those achievable when cross-matching radio positions, as well as mid-IR and optical ones (when available), with X-ray sources listed in the clean sample of the Second Swift-XRT Point Source Catalog[37] (2SXPS; Evans et al. 2020). The only differences we found are summarized below:

1. For four sources, namely G4Jy 27, G4Jy 446, G4Jy 854, and G4Jy 1757, all marked with XDF = *u*, there is a counterpart listed in the 2SXPS catalog found within the X-ray positional uncertainty at the 90% level of confidence and having an X-ray position consistent with their radio core. We also reported their X-ray detection based on the run carried out with the SOSTA algorithm having relatively low values of the S/N, below the threshold adopted for the DET algorithm. This difference is based on the fact that the 2SXPS catalog used a lower threshold on the S/N to claim a detection. Moreover the 2SXPS catalog is built by reducing Swift-XRT observations with nominal $T_{\rm exp}$ lower than the threshold of 250 s adopted here.
2. Two more sources, namely G4Jy 45 and G4Jy 1038 (aka 3C 279), have an X-ray counterpart listed in the 2SXPS

[37] https://heasarc.gsfc.nasa.gov/W3Browse/swift/swift2sxps.html

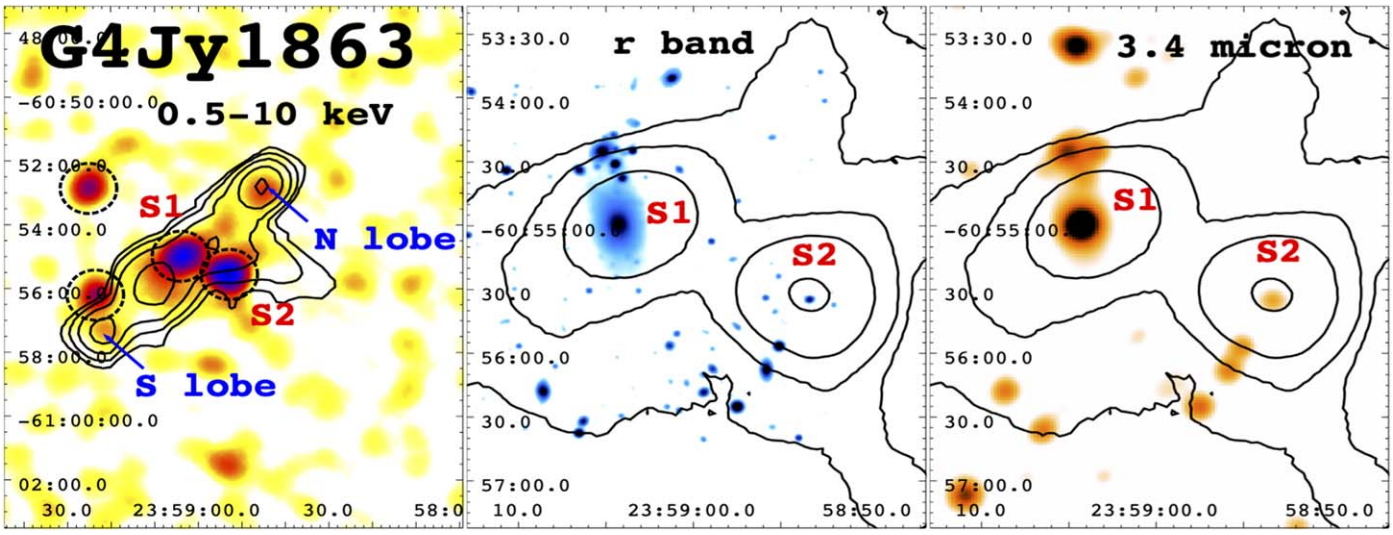

Figure 5. The X-ray image (left panel), smoothed with a Gaussian kernel of 42.″426, for the radio source G4Jy 1863. Radio contours are drawn using a radio map at 843 MHz starting at the level of 90 mJy beam^{-1} and increasing by a factor of 3. Black circles, of 20 pixel radius, mark the location of point-like sources detected at an S/N < 3, while blue arrows mark the locations of both the northern (N) and the southern (S) radio lobe. The X-ray counterpart of the radio core (S1) and that of the nearby companion galaxy (S2) have a clear counterpart in the optical (*r*-band) image retrieved from DES *r* band (central panel) as well as at mid-IR frequencies at 3.4 μm obtained with the Wide-field Infrared Survey Explorer (WISE) All-sky survey (right panel). X-ray intensity contours, obtained from the Swift-XRT event files and drawn starting at a level of 0.01 photons, are overlaid onto both the optical and the mid-IR images to help identifying the location of the low-energy counterparts to S1 and S2. The X-ray emission of both the northern and the southern radio lobes is detected, above a 3σ level of confidence, comparing the number of photons measured within a circular region, of 20 pixel radius, centered on their radio intensity peak and that expected, on average, on a background region of the same area.

catalog that we did not analyze here. G4Jy 45 has XRT observations beyond the threshold of 10′ separation set to select sources and thus was automatically excluded when retrieving data sets from the Swift archive. G4Jy 1038, as previously stated, was not selected as it is extensively discussed in the literature.

We also compared our results with those recently presented by Maselli et al. (2022), who analyzed Swift observations of 31 radio sources listed in the SMS4 catalog (Burgess & Hunstead 2006a, 2006b), 22 in common with our sample. Our results are in agreement with those presented Maselli et al. (2022). For ten sources (G4Jy 93, G4Jy 249, G4Jy 506, G4Jy 563, G4Jy 672, G4Jy 723, G4Jy 950, G4Jy 1135, G4Jy 1192, and G4Jy 1432), we detect the same X-ray counterpart, while G4Jy 257, G4Jy 293, G4Jy 416, G4Jy 718, and G4Jy 836, all marked as XDF = *u* according to our analysis, have only upper limits on their X-ray count rates measured by Maselli et al. (2022). Moreover, as occurred when comparing our results with those of the 2SXPS catalog, for five sources, namely G4Jy 27, G4Jy 446, G4Jy 580, G4Jy 854, and G4Jy 1203, we detected an X-ray counterpart only by using the SOSTA algorithm, the same procedure adopted by Maselli et al. (2022).

Finally, the only difference between our analysis and that of the 2SXPS catalog and/or the literature (i.e., Maselli et al. 2022) is for G4Jy 20, which is marginally detected in both analyses but undetected in our investigation. The main reason is due to the threshold on $T_{\rm exp}$ chosen to retrieve Swift-XRT archival observations. Including all data sets with nominal $T_{\rm exp}$ above 50 s we also found a marginal detection when adopting the SOSTA algorithm, with S/N = 1.6 in agreement with previous analyses.

6. Mid-IR and Optical Counterparts Identified with X-Ray Observations

We also compared the results of the X-ray analysis with those obtained from the search for optical counterparts, and all results of this comparison are summarized as follows:

1. For the radio source G4Jy 672, with an assigned mid-IR counterpart reported in Paper I, the X-ray counterpart lies within an angular separation of ∼2″ from the optical host galaxy, thus confirming its previous association.
2. There are two more sources, namely G4Jy 249 and G4Jy 1432 (see Figure 6), for which available radio maps lack the angular resolution needed to locate their radio cores precisely and consequently their host galaxies in the optical band. However, using the Swift-XRT images it has been possible to determine the position of their optical counterparts using their X-ray emission. We are also able to confirm that the X-ray-detected sources are spatially coincident with their mid-IR counterparts associated in the G4Jy catalog.
3. Despite the lack of a potential optical counterpart, the X-ray emission of G4Jy 1136 is spatially associated with its mid-IR counterpart (see also Figure 7) as previously stated in the G4Jy catalog (White et al. 2020a, 2020b). On the other hand, the comparison with mid-IR, optical, and X-ray data carried out for G4Jy 1192 revealed the location of its optical host galaxy, as shown in the right panel of Figure 8, in agreement with the mid-IR association described in Paper I.

7. Summary, Conclusions, and Future Perspectives

In this second paper of the series, we present a first overview of the X-ray archival observations for G4Jy-3CRE radio sources, mainly focusing on those observed with the XRT instrument on board the Neil Gehrels Swift Observatory.

The G4Jy-3CRE sample was recently extracted from the G4Jy catalog (White et al. 2020a, 2020b) to obtain a list of powerful radio sources, selected at low radio frequencies, equivalent, in terms of flux density, to the 3C catalog but having all sources located in the Southern Hemisphere (Paper I). The main advantage underlying the selection of this sample is the opportunity to study powerful radio sources and

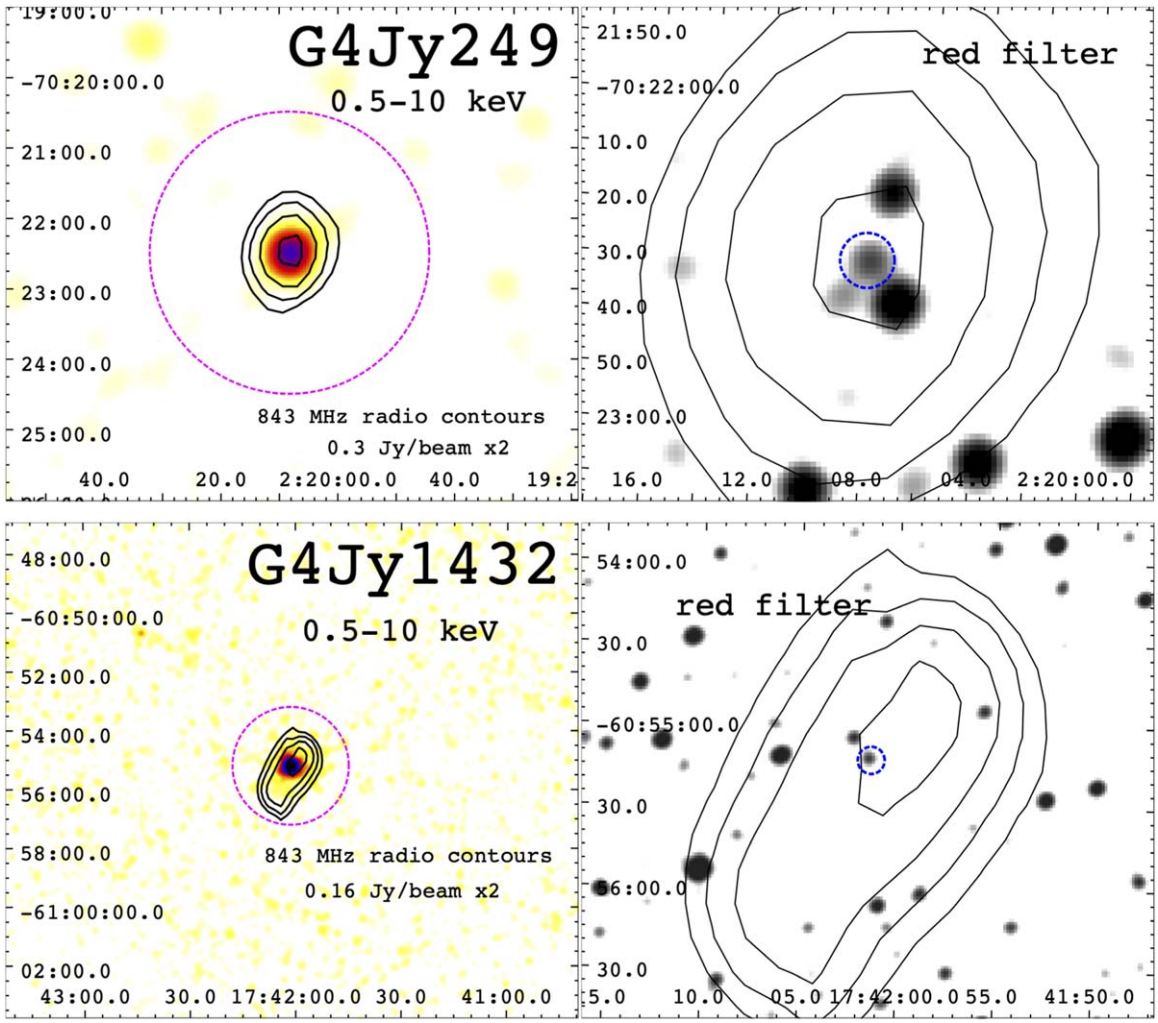

Figure 6. Upper panels: the left image is obtained from the merged XRT event files, smoothed with a Gaussian kernel of 10 pixels (i.e., $23\farcs57$), as in Figure 2, while the right one is the optical image retrieved from the DSS archive in the red filter. The blue circle in the right panel is centered on the location of the X-ray counterpart to mark its position and that of the corresponding host galaxy. Radio contours are overlaid onto both images drawn at the frequency indicated (i.e., 843 MHz obtained from the SUMSS archive) together with the intensity of the first contour level and increasing in level by a binning factor of 2. Lower panels: same as the upper panels but for the radio source G4Jy 1432. Thanks to this optical-to-X-ray comparison we have been able to distinguish which source is the optical counterpart for these two radio sources having radio maps with insufficient angular resolution to locate precisely the radio core. The cyan cross marks the location of the radio source (i.e., brightness-weighted radio centroid as reported in the G4Jy catalog) while the red cross marks the mid-IR-assigned counterpart, associated in the analysis of the G4Jy sample.

emission processes occurring in their large-scale environments with a catalog observable with modern Southern Hemisphere telescopes and instruments such as MUSE and ERIS at VLT and/or ALMA and, in the near future, also SKA, LSST, and ELT.

We retrieved, reduced, and analyzed all archival Swift-XRT data sets collected between 2005 May and 2022 December, having nominal $T_{\rm exp}$ larger than 250 s for a total of 624 observations processed for 89 sources. We found 30 radio sources with no X-ray counterpart detected above the chosen threshold of $S/N = 3$. We found nine radio sources with extended/diffuse X-ray emission, estimated according to the criterion based on the Swift-XRT PSF model. In particular, G4Jy 1518 and G4Jy 1664 show clear extended X-ray emission, previously unknown, suggesting that they could be hosted in galaxy clusters, while for G4Jy 1863 we claim the X-ray counterpart detection of its radio lobes. All remaining 50 radio sources have a detected X-ray point-like counterpart of their radio core. The main reason underlying the nondetection of X-ray counterparts for all radio sources analyzed here is due to their relatively short integrated $T_{\rm exp}$.

Swift X-ray observations can provide first insights into the presence of diffuse/extended X-ray emission, used as the basis for future studies, and also to (i) confirm previous mid-IR and optical associations and to (ii) locate precisely the host galaxy position for those sources for which the angular resolution of the radio maps was not sufficient to reveal the position of the radio core.

We also obtained additional results that refine our previous radio-to-optical comparison (Paper I):

1. For G4Jy 672, having no assigned mid-IR counterpart in the original G4Jy catalog, the X-ray counterpart lies within an angular separation of $\sim 2''$ from the optical host galaxy, thus confirming its optical association since it is smaller than the typical Swift-XRT positional uncertainty for that $T_{\rm exp}$ (see, e.g., Evans et al. 2020). There is further confirmation of the host galaxy position via detection of

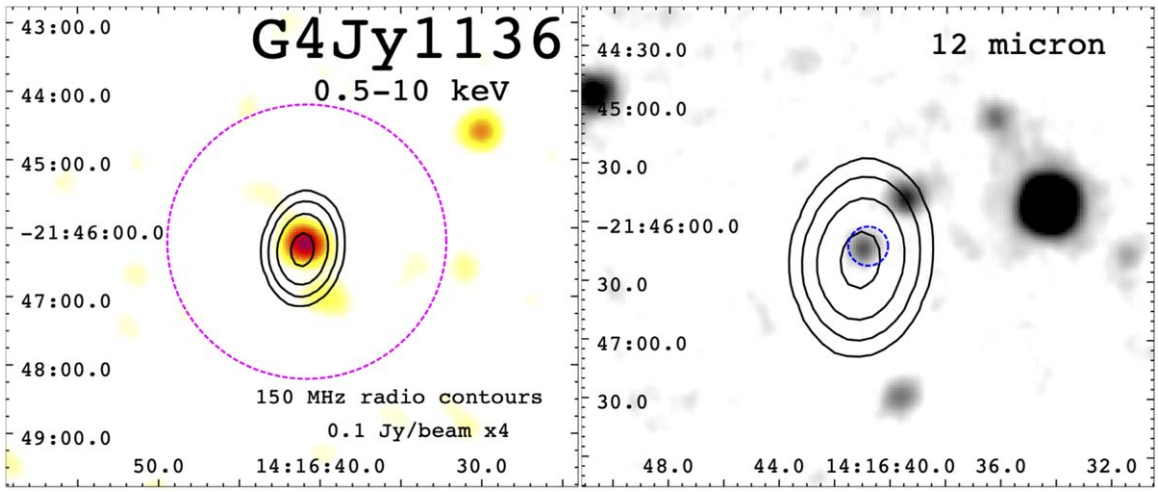

Figure 7. Left panel: the X-ray image of G4Jy 1136 obtained from the merged XRT event file as in Figure 2, smoothed with a Gaussian kernel of 10 pixels (i.e., $23\farcs57$) and with radio contours drawn from the TGSS radio map overlaid. These were computed starting at level of 0.1 Jy beam^{-1} and increasing in level by a binning factor of 4. Right panel: the same field but observed as part of the WISE All-sky survey at 12 μm. The magenta dashed circle in the right panel is centered on the location of the X-ray counterpart to mark its position and that the mid-IR associated source (position indicated by the red cross in the right panel). According to our previous analysis (Paper I) this radio source lacks an optical counterpart but the Swift-XRT analysis revealed that the mid-IR counterpart assigned in the G4Jy catalog is correct as it overlaps with its X-ray counterpart. It is worth highlighting the presence of a relatively bright star located in the northwestern direction with respect to the position of G4Jy 1136. However it appears fainter in the 12 μm WISE image, shown here, rather than in that at 3.4 μm used in Paper I. A cyan cross, if present, marks the location of the radio source (i.e., brightness-weighted radio centroid as reported in the G4Jy catalog) while the red one that of the assigned mid-IR counterpart associated in the analysis of the G4Jy sample.

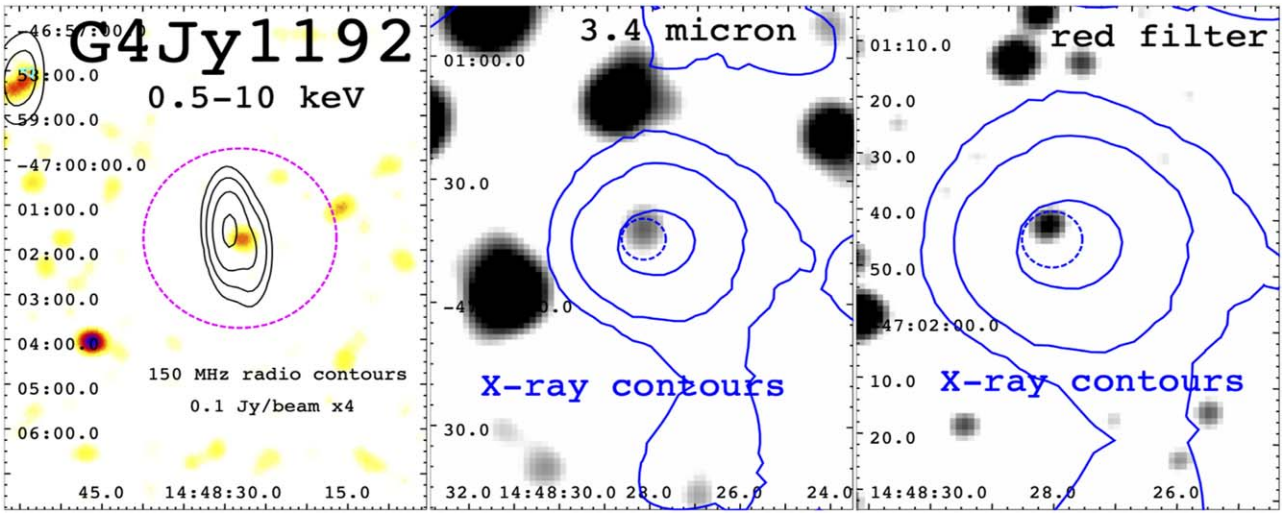

Figure 8. Left panel: the X-ray image of G4Jy 1192 obtained from the merged XRT event file smoothed with a Gaussian kernel of 10 pixels (i.e., $23\farcs57$), as in Figure 2 and in Figure 7, with radio contours drawn from the TGSS radio map overlaid. These contours were computed starting at level of 0.1 Jy beam^{-1} and increase in level by a binning factor of 4. Middle and right panels: the same field but observed as part of the WISE All-sky survey at 3.4 μm and in the red filter collected from the DSS archive, respectively. The magenta dashed circle in the left panel is centered on the location of the X-ray counterpart to mark its position, the same is marked by the blue dashed circles in the other two panels, while the cyan cross marks the location of the radio source (i.e., brightness-weighted radio centroid) as reported in the G4Jy catalog. In our previous analysis (Paper I) G4Jy 1192 lacks both mid-IR and optical counterparts. However, thanks to the Swift-XRT analysis, we have been able to identify these counterparts. X-ray contours obtained from the image in the left panel are overlaid onto both the mid-IR and optical images for comparison.

the radio core in a recent MeerKAT image (Sejake et al. 2023).

2. Our previous radio-to-optical comparison did not allow us to establish firmly the host galaxies of G4Jy 249 and G4Jy 1432 due to the relatively poor angular resolution of the radio maps used to locate their radio cores. However, using merged Swift-XRT images we determined precisely the locations of their optical counterparts from their X-ray emission.
3. We also confirmed that the X-ray emission of G4Jy 1136 is spatially associated with its assigned mid-IR counterpart as listed in the original G4Jy catalog.
4. The mid-IR, optical, and X-ray comparison carried out for G4Jy 1192 also revealed the location of its optical host galaxy.

Swift-XRT archival data sets, even if not homogeneous in terms of integrated $T_{\rm exp}$ that span a range between 5 and 96 ks, proved to be a powerful tool to refine the optical search for host galaxies of powerful radio sources and discover the presence of extended X-ray emission. In the cases of G4Jy 1518 and G4Jy 1664, having snapshot XRT observations of $\sim$4 and $\sim$2 ks integrated $T_{\rm exp}$, it has been possible to reveal the presence of the surrounding ICM.

Swift-XRT observations are certainly paving the path to identify those radio sources deserving X-ray follow-up observations to perform detailed X-ray spectral analyses. This is crucial to complete optical spectroscopic observations necessary to (i) obtain the z measurements for the whole G4Jy-3CRE catalog and (ii) classify all radio sources listed therein from an optical perspective.

Additional X-ray data sets have been already requested and approved for the XMM-Newton satellite, as "filler programs" and as snapshot observations, to achieve a more complete high-energy overview of the G4Jy-3CRE catalog, while follow-up X-ray observations will be also requested in the near future to investigate deeply the large-scale environment of those radio sources harbored in galaxy clusters/groups.

Acknowledgments

We thank the anonymous referee for useful and valuable comments and suggestions that led to improvements in the paper. We wish to dedicate this paper to D. E. Harris and R. W. Hunstead, their insight, passion, and contributions to radio astronomy are an inspiration for most of us.

F.M. wishes to thank Dr. A. Moretti for their valuable discussions on the Swift-XRT PSF models and for all useful suggestions provided.

A.J. acknowledges the financial support (MASF_CONTR_-FIN_18_01) from the Italian National Institute of Astrophysics under the agreement with the Instituto de Astrofisica de Canarias for the "Becas Internacionales para Licenciados y/o Graduados Convocatoria de 2017." S.V.W. acknowledges financial assistance of the South African Radio Astronomy Observatory (SARAO; https://www.sarao.ac.za). W.F. and R.K. acknowledge support from the Smithsonian Institution and the Chandra High Resolution Camera Project through NASA contract NAS8-03060. W.F. also acknowledges support from NASA Grants 80NSSC19K0116, GO1-22132X, and GO9-20109X. This investigation is supported by the National Aeronautics and Space Administration (NASA) grants GO9-20083X, GO0-21110X and GO1-22087X. I.A., S.A. C. and V.R. are partially supported by grant PIP 1220200102169CO, Argentine Research Council (CONICET), and by the UNLP research project, G178 (2022-2025). A.G.-P. acknowledges support from the CONACyT program for their PhD studies. V.C. acknowledges support from the Fulbright — García Robles scholarship. This work was partially supported by CONACyT (Consejo Nacional de Ciencia y Tecnología) research grant 280789.

This research has made use of the NASA/IPAC Extragalactic Database (NED), which is operated by the Jet Propulsion Laboratory, California Institute of Technology, under contract with the National Aeronautics and Space Administration. This research has made use of the SIMBAD database, operated at CDS, Strasbourg, France (Wenger et al. 2000).

This research has made use of the CIRADA cutout service at https://cutouts.cirada.ca, operated by the Canadian Initiative for Radio Astronomy Data Analysis (CIRADA). CIRADA is funded by a grant from the Canada Foundation for Innovation 2017 Innovation Fund (Project 35999), as well as by the Provinces of Ontario, British Columbia, Alberta, Manitoba and Quebec, in collaboration with the National Research Council of Canada, the US National Radio Astronomy Observatory and Australia's Commonwealth Scientific and Industrial Research Organisation. The National Radio Astronomy Observatory is a facility of the National Science Foundation operated under cooperative agreement by Associated Universities, Inc. Part of this work is based on the NVSS (NRAO VLA Sky Survey): The National Radio Astronomy Observatory is operated by Associated Universities, Inc., under contract with the National Science Foundation and on the VLA low-frequency Sky Survey (VLSS). We thank the staff of the GMRT that made these observations possible. GMRT is run by the National Centre for Radio Astrophysics of the Tata Institute of Fundamental Research. The Molonglo Observatory site manager, Duncan Campbell-Wilson, and the staff, Jeff Webb, Michael White, and John Barry, are responsible for the smooth operation of Molonglo Observatory Synthesis Telescope (MOST) and the day-to-day observing program of SUMSS. The SUMSS survey is dedicated to Michael Large whose expertise and vision made the project possible. The MOST is operated by the School of Physics with the support of the Australian Research Council and the Science Foundation for Physics within the University of Sydney. This scientific work makes use of the Murchison Radio-astronomy Observatory, operated by CSIRO. We acknowledge the Wajarri Yamatji people as the traditional owners of the Observatory site. Support for the MWA comes from the US National Science Foundation (grants AST-0457585, PHY-0835713, CAREER-0847753, and AST-0908884), the Australian Research Council (LIEF grants LE0775621 and LE0882938), the US Air Force Office of Scientific Research (grant FA9550-0510247), and the Centre for All-sky Astrophysics (an Australian Research Council Centre of Excellence funded by grant CE110001020). Support is also provided by the Smithsonian Astrophysical Observatory, the MIT School of Science, the Raman Research Institute, the Australian National University, and the Victoria University of Wellington (via grant MED-E1799 from the New Zealand Ministry of Economic Development and an IBM Shared University Research Grant). The Australian Federal government provides additional support via the Commonwealth Scientific and Industrial Research Organisation (CSIRO), National Collaborative Research Infrastructure Strategy, Education Investment Fund, and the Australia India Strategic Research Fund, and Astronomy Australia Limited, under contract to Curtin University. This work was supported by resources provided by the Pawsey Supercomputing Centre with funding from the Australian Government and the Government of Western Australia. We acknowledge the iVEC Petabyte Data Store, the Initiative in Innovative Computing, and the CUDA Center for Excellence sponsored by NVIDIA at Harvard University, and the International Centre for Radio Astronomy Research (ICRAR), a Joint Venture of Curtin University, and The University of Western Australia, funded by the Western Australian State government.

This publication makes use of data products from the Wide-field Infrared Survey Explorer, which is a joint project of the University of California, Los Angeles, and the Jet Propulsion Laboratory/California Institute of Technology, funded by the National Aeronautics and Space Administration.

This project used public archival data from the Dark Energy Survey (DES). Funding for the DES Projects has been provided by the U.S. Department of Energy, the U.S. National Science Foundation, the Ministry of Science and Education of Spain, the Science and Technology Facilities Council of the United Kingdom, the Higher Education Funding Council for England, the National Center for Supercomputing Applications at the University of Illinois at Urbana-Champaign, the Kavli Institute of Cosmological Physics at the University of Chicago, the Center for Cosmology and Astro-Particle Physics at the Ohio State University, the Mitchell Institute for Fundamental Physics

and Astronomy at Texas A&M University, Financiadora de Estudos e Projetos, Fundação Carlos Chagas Filho de Amparo à Pesquisa do Estado do Rio de Janeiro, Conselho Nacional de Desenvolvimento Científico e Tecnológico and the Ministério da Ciência, Tecnologia e Inovação, the Deutsche Forschungsgemeinschaft, and the Collaborating Institutions in the Dark Energy Survey. The Collaborating Institutions are Argonne National Laboratory, the University of California at Santa Cruz, the University of Cambridge, Centro de Investigaciones Energéticas, Medioambientales y Tecnológicas-Madrid, the University of Chicago, University College London, the DES-Brazil Consortium, the University of Edinburgh, the Eidgenössische Technische Hochschule (ETH) Zürich, Fermi National Accelerator Laboratory, the University of Illinois at Urbana-Champaign, the Institut de Ciències de l'Espai (IEEC/CSIC), the Institut de Física d'Altes Energies, Lawrence Berkeley National Laboratory, the Ludwig-Maximilians Universität München and the associated Excellence Cluster Universe, the University of Michigan, the National Optical Astronomy Observatory, the University of Nottingham, the Ohio State University, the OzDES Membership Consortium, the University of Pennsylvania, the University of Portsmouth, SLAC National Accelerator Laboratory, Stanford University, the University of Sussex, and Texas A&M University. Based in part on observations at Cerro Tololo Inter-American Observatory, National Optical Astronomy Observatory, which is operated by the Association of Universities for Research in Astronomy (AURA) under a cooperative agreement with the National Science Foundation. The Pan-STARRS1 Surveys (PS1) have been made possible through contributions of the Institute for Astronomy, the University of Hawaii, the Pan-STARRS Project Office, the Max-Planck Society and its participating institutes, the Max Planck Institute for Astronomy, Heidelberg and the Max Planck Institute for Extraterrestrial Physics, Garching, The Johns Hopkins University, Durham University, the University of Edinburgh, Queen's University Belfast, the Harvard-Smithsonian Center for Astrophysics, the Las Cumbres Observatory Global Telescope Network Incorporated, the National Central University of Taiwan, the Space Telescope Science Institute, the National Aeronautics and Space Administration under grant No. NNX08AR22G issued through the Planetary Science Division of the NASA Science Mission Directorate, the National Science Foundation under grant No. AST-1238877, the University of Maryland, and Eotvos Lorand University (ELTE). Based on photographic data obtained using The UK Schmidt Telescope. The UK Schmidt Telescope was operated by the Royal Observatory Edinburgh, with funding from the UK Science and Engineering Research Council, until 1988 June, and thereafter by the Anglo-Australian Observatory. Original plate material is copyright (c) of the Royal Observatory Edinburgh and the Anglo-Australian Observatory. The plates were processed into the present compressed digital form with their permission. The Digitized Sky Survey was produced at the Space Telescope Science Institute under US Government grant NAG W-2166. We acknowledge the efforts of the staff of the Anglo-Australian Observatory, who have undertaken the observations and developed the 6dF instrument. This data set or service is made available by the Infrared Science Archive (IRSA) at IPAC, which is operated by the California Institute of Technology under contract with the National Aeronautics and Space Administration.

SAO Image DS9 development has been made possible by funding from the Chandra X-ray Science Center (CXC), the High Energy Astrophysics Science Archive Center (HEASARC), and the JWST Mission office at Space Telescope Science Institute (Joye & Mandel 2003). This research has made use of data obtained from the High-Energy Astrophysics Science Archive Research Center (HEASARC) provided by NASA Goddard Space Flight Center. We acknowledge the use of NASA's SkyView facility (http://skyview.gsfc.nasa.gov) located at NASA Goddard Space Flight Center. TOPCAT and STILTS astronomical software (Taylor 2005) were used for the preparation and manipulation of the tabular data and the images. The analysis is partially based on the OCCAM computing facility hosted by C3S (http://c3s.unito.it/) at UniTO (Aldinucci et al. 2017).

Appendix
Swift–Chandra Comparison

Four G4Jy-3CRE radio sources in the selected sample have X-ray observations in the Chandra archive that are still unpublished but publicly available. Thus we retrieved those data sets and we compare the Swift-XRT and Chandra event files. There are other G4Jy-3CRE radio sources observed with Chandra but these data sets were all already discussed in the literature (see, e.g., individual notes for the G4Jy-3CRE catalog in Appendix B of Paper I for more details).

Data reduction procedures adopted for Chandra observations are extensively described in our previous papers (see, e.g., Massaro et al. 2009a, 2009b, 2011; Jimenez-Gallardo et al. 2021; and references therein for more details). Here we followed the standard procedure described in the Chandra Interactive Analysis of Observations (CIAO) threads[38] and we used CIAO v4.14 with the Chandra Calibration Database (CALDB) version 4.9.6. to generate level 2 event files. These were obtained using the *acis_process_events* task of Chandra textsubscriptre.pro script, and events were filtered for grades 0, 2, 3, 4, and 6. Light curves were also extracted and inspected for every data set to verify the absence of high-background intervals. Such time intervals were never found in the selected observations. The four radio sources analyzed here, namely G4Jy 171, G4Jy 260, G4Jy 411, and G4Jy 1613, were observed with the ACIS-S detector in VFAINT mode. In particular G4Jy 171 was observed twice (obs. ID numbers 16099 and 17577) but we only reduced the longer observation (25 ks nominal $T_{\rm exp}$) carried out on 2015 February 2, while G4Jy 260 (obs. ID 21488, 2020 October 17, 10 ks), G4Jy 411 (obs. ID 23098, 2019 December 12, 10 ks) and G4Jy 1613 (obs. ID 23177, 2020 February 25, 10 ks) where all pointed one time with Chandra, the last two being selected as cool attitude targets.[39]

In Figure 9 we show a comparison between the Swift-XRT event file, as shown in Figure 2, with the Chandra level 2 event file restricted in the 0.5–7 keV band. We found that the Chandra X-ray image of G4Jy 260 clearly shows a readout streak (north–south direction) due to the presence of pileup (see, e.g., Davis 2001; McCollough & Rots 2005; and references therein) but we discovered that the radio hotspot, located on the western side of the nucleus, has an X-ray counterpart. Then we detected the X-ray counterpart of all radio cores for these four G4Jy-3CRE sources, thus confirming the

[38] http://cxc.harvard.edu/ciao/guides/index.html
[39] https://cxc.harvard.edu/proposer/CCTs.html

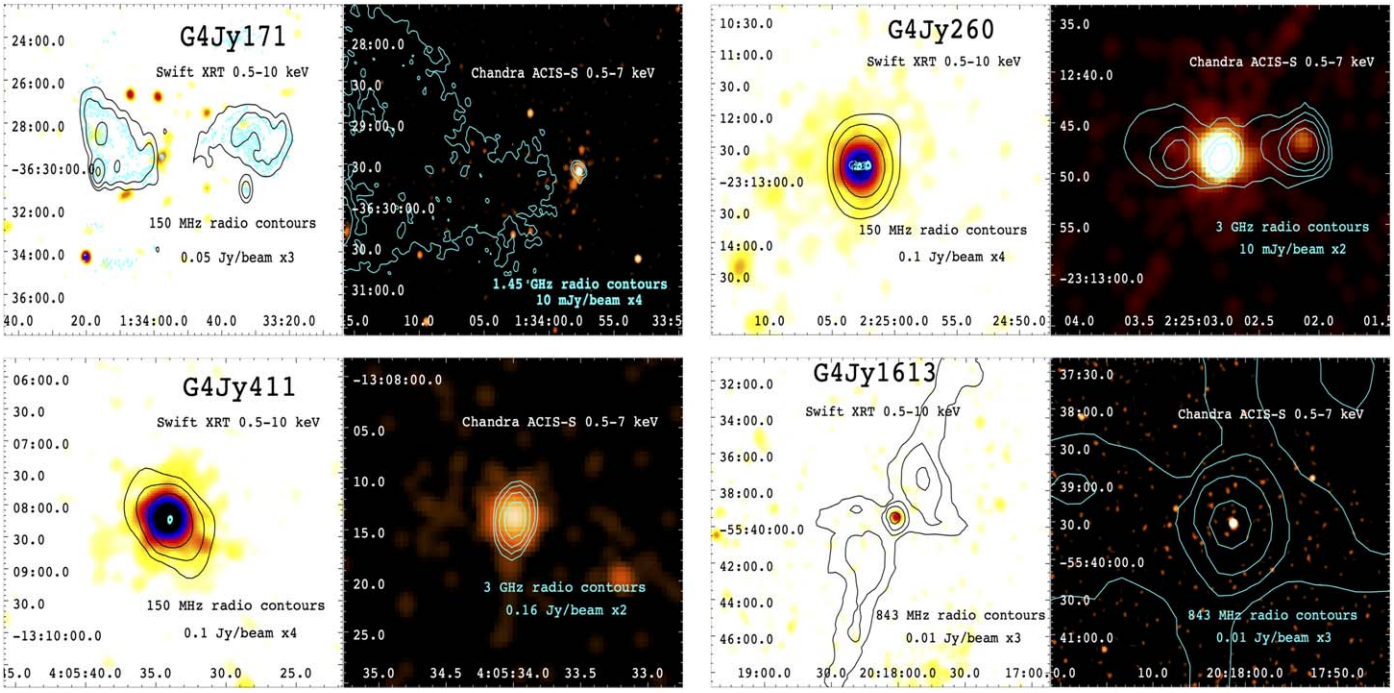

Figure 9. Left panels: Swift-XRT images. Right panels: Chandra images obtained from event files restricted in the 0.5–7 keV energy range. Radio contours at different frequencies are overlaid in black onto the Swift images and in cyan in both panels. The frequency of the radio maps from which the radio contours were drawn are reported in each panel together with the intensity of the first level and the binning factor.

Swift-XRT results. Finally, no clear signatures of extended X-ray emission were found in these Chandra data sets, with the only exception of a marginal detection of diffuse X-ray radiation around G4 Jy171.

ORCID iDs

F. Massaro https://orcid.org/0000-0002-1704-9850
S. V. White https://orcid.org/0000-0002-2340-8303
A. Paggi https://orcid.org/0000-0002-5646-2410
A. Jimenez-Gallardo https://orcid.org/0000-0003-4413-7722
C. Mazzucchelli https://orcid.org/0000-0002-5941-5214
W. R. Forman https://orcid.org/0000-0002-9478-1682
A. Capetti https://orcid.org/0000-0003-3684-4275
A. García-Pérez https://orcid.org/0000-0002-9896-6430
C. C. Cheung https://orcid.org/0000-0002-4377-0174
V. Chavushyan https://orcid.org/0000-0002-2558-0967
N. P. H. Nesvadba https://orcid.org/0000-0001-5783-6544
I. Andruchow https://orcid.org/0000-0003-1562-5188
H. A. Peña-Herazo https://orcid.org/0000-0003-0032-9538
E. Sani https://orcid.org/0000-0002-3140-4070
R. Grossová https://orcid.org/0000-0003-3471-7459
V. Reynaldi https://orcid.org/0000-0002-6472-6711
R. P. Kraft https://orcid.org/0000-0002-0765-0511
B. Balmaverde https://orcid.org/0000-0002-0690-0638
S. Cellone https://orcid.org/0000-0002-3866-2726

References

Abbott, T. M. C., Abdalla, F. B., Allam, S., et al. 2018, ApJS, 239, 18
Abdollahi, S., Acero, F., Ackermann, M., et al. 2020, ApJS, 247, 33
Abell, G. O. 1958, ApJS, 3, 211
Abell, G. O., Corwin, H. G., Jr., & Olowin, O. P. 1989, ApJS, 70, 1
Ahn, C. P., Alexandroff, R., Allende, P. C., et al. 2012, ApJS, 203, 21
Aldinucci, M., Bagnasco, S., Lusso, S., et al. 2017, JPhCS, 898, 082039
Bacon, R., Accardo, M., Adjali, L., et al. 2010, Proc. SPIE, 7735, 773508
Bagchi, J., Pislar, V., & Lima Neto, G. B. 1998, MNRAS, 296, L23
Baldi, R. D., Chiaberge, M., Capetti, A., et al. 2010, ApJ, 725, 2426
Baldwin, A. J. 1975, ApJ, 201, 26
Balmaverde, B., Capetti, A., Baldi, R. D., et al. 2022, A&A, 662, A23
Balmaverde, B., Capetti, A., Grandi, P., et al. 2012, A&A, 545, A143
Balmaverde, B., Capetti, A., Marconi, A., et al. 2018, A&A, 619, A83
Balmaverde, B., Capetti, A., Marconi, A., et al. 2019, A&A, 632, A124
Balmaverde, B., Capetti, A., Marconi, A., et al. 2021, A&A, 645, A12
Balmaverde, B., Capetti, A., Marconi, A., & Venturi, G. 2018, A&A, 612, A19
Begelman, M. C., Blandford, R. D., & Rees, M. J. 1984, RvMP, 56, 255
Bennett, A. S. 1962, MmRAS, 68, 163
Bennett, C. L., Larson, D., Weiland, J. L., & Hinshaw, G. 2014, ApJ, 794, 135
Bergeron, J., & Kunth, D. 1984, MNRAS, 207, 263
Best, P. N., Röttgering, H. J. A., & Lehnert, M. D. 1999, MNRAS, 310, 223
Best, P. N., Röttgering, H. J. A., & Lehnert, M. D. 2000, MNRAS, 315, 21
Birkinshaw, M., Worrall, D. M., & Hardcastle, M. J. 2002, MNRAS, 335, 142
Borne, K. D., & Hoessel, J. G. 1984, BAAS, 16, 881
Browne, L. W. A., & Savage, A. 1977, MNRAS, 179, 65P
Bruni, G., Panessa, F., Bassani, L., et al. 2020, MNRAS, 494, 902
Burbidge, E. M. 1967, ApJL, 149, L51
Burbidge, E. M., & Burbidge, G. R. 1972, ApJ, 172, 37
Burbidge, E. M., & Kinman, T. D. 1966, ApJ, 145, 654
Burgess, A. M., & Hunstead, R. W. 2006a, AJ, 131, 100
Burgess, A. M., & Hunstead, R. W. 2006b, AJ, 131, 114
Burns, J. O. 1981, MNRAS, 195, 523
Burrows, D., Hill, J. E., Nousek, J. A., et al. 2005, SSRv, 120, 165
Burrows, D. N., Hill, J. E., Nousek, J. A., et al. 2000, Proc. SPIE, 4140, 64
Buttiglione, S., Capetti, A., Celotti, A., et al. 2009, A&A, 495, 1033
Buttiglione, S., Capetti, A., Celotti, A., et al. 2010, A&A, 509, A6
Buttiglione, S., Capetti, A., Celotti, A., et al. 2011, A&A, 525A, 28
Capalbi, M., Perri, M., Saija, B., & Tamburelli, F. 2005, ASI Science Data Center, 1
Carter, D., & Malin, D. F. 1983, MNRAS, 203, 49P
Cava, A., Bettoni, D., Poggianti, B. M., et al. 2009, A&A, 495, 707
Chiaberge, M., Capetti, A., & Celotti, A. 2000, A&A, 355, 873
Chiaberge, M., Gilli, R., Lotz, J. M., & Norman, C. 2015, ApJ, 806, 147
Cohen, A. S., Lane, W. M., Cotton, W. D., et al. 2007, AJ, 134, 1245
Collmar, W., Böttcher, M., Krichbaum, T. P., et al. 2010, A&A, 522, A66
Condon, J. J., Cotton, W. D., Greisen, E. W., et al. 1998, AJ, 115, 1693
Condon, J. J., Cotton, W. D., White, S. V., et al. 2021, ApJ, 917, 18
Croston, J. H., Hardcastle, M. J., Harris, D. E., et al. 2005, ApJ, 626, 733

Cusumano, G., La Parola, V., Segreto, A., et al. 2010, A&A, 524, A64
Dai, X., Griffin, R. D., Kochanek, C. S., Nugent, J. M., & Bregman, J. N. 2015, ApJS, 218, 8
Danziger, I. J., & Goss, W. M. 1983, MNRAS, 202, 703
Davis, J. E. 2001, ApJ, 562, 575
de Koff, S., Baum, S. A., Sparks, W. B., et al. 1996, ApJS, 107, 621
D'Elia, V., Perri, M., Puccetti, S., et al. 2013, A&A, 551, A142
Dicken, D., Tadhunter, C., Morganti, R., et al. 2014, ApJ, 788, 98
di Serego Alighieri, S., Danziger, I. J., Morganti, R., & Tadhunter, C. N. 1994, MNRAS, 269, 998
Djorgovski, S., Spinrad, H., McCarthy, P., et al. 1988, AJ, 96, 836
Ebeling, H., Voges, W., Bohringer, H., et al. 1996, MNRAS, 281, 799
Edge, D. O., Shakeshaft, J. R., McAdam, W. B., Baldwin, J. E., & Archer, S. 1959, MmRAS, 68, 37
Efstathiou, G., Ellis, R. S., & Carter, D. 1980, MNRAS, 193, 931
Ellingson, E. 1988, BAAS, 20, 1025
Ellingson, E., Green, R. F., & Yee, H. K. C. 1987, BAAS, 19, 685
Ellingson, E., Green, R. F., & Yee, H. K. C. 1991, ApJ, 378, 476
Ellingson, E., Yee, H. K. C., Green, R. F., & Kinman, T. D. 1989, AJ, 97, 1539
Evans, D. A., Worrall, D. M., Hardcastle, M. J., et al. 2006, ApJ, 642, 96
Evans, P. A., Osborne, J. P., Beardmore, A. P., et al. 2014, ApJS, 210, 8
Evans, P. A., Page, K. L., Osborne, J. P., et al. 2020, ApJS, 247, 54
Fabian, A. C. 2012, ARA&A, 50, 455
Flewelling, H. A., Magnier, E. A., Chambers, K. C., et al. 2020, ApJS, 251, 7
Gehrels, N., Chincarini, G., Giommi, P., et al. 2004, ApJ, 611, 1005
Giommi, P., Angelini, L., Jacobs, P., & Tagliaferri, G. 1992, in ASP Conf. Ser. 25, Astronomical Data Analysis Software and Systems I, ed. D. M. Worrall, C. Biemesderfer, & J. Barnes (San Francisco, CA: ASP), 100
Giovannini, G., Taylor, G. B., Feretti, L., et al. 2005, ApJ, 618, 635
Grossová, R., Werner, N., Massaro, F., et al. 2022, ApJS, 258, 30
Grossová, R., Werner, N., Rajpurohit, K., et al. 2019, MNRAS, 488, 1917
Hardcastle, M. J., Birkinshaw, M., Cameron, R. A., et al. 2002, ApJ, 581, 948
Hardcastle, M. J., & Croston, J. H. 2020, NewAR, 88, 101539
Hardcastle, M. J., Evans, D. A., & Croston, J. H. 2006, MNRAS, 370, 1893
Hardcastle, M. J., & Worrall, D. M. 2000, MNRAS, 314, 359
Harris, D. E., & Grindlay, J. E. 1979, MNRAS, 188, 25
Harris, D. E., & Krawczynski, H. 2006, ARA&A, 44, 463
Harvanek, M., Ellingson, E., Stocke, J. T., et al. 2001, AJ, 122, 2874
Hayashida, M., Nalewajko, K., Madejski, G. M., et al. 2015, ApJ, 807, 79
HI4PI Collaboration, Ben Bekhti, N., Floer, L., et al. 2016, A&A, 594, A116
Hilbert, B., Chiaberge, M., Kotyla, J. P., et al. 2016, ApJS, 225, 12
Hilker, M., Infante, L., Vieira, G., Kissler-Patig, M., & Richtler, T. 1999, A&AS, 134, 75
Hill, J. E., Burrows, D. N., Nousek, J. A., et al. 2004, Proc. SPIE, 5165, 217
Hiltner, P. R., & Roeser, H. J. 1991, A&A, 244, 37
Hintzen, P., Ulvestad, J., & Owen, F. 1983, AJ, 88, 709
Ho, L. C., & Kim, M. 2009, ApJS, 184, 398
Hoopes, C. G., Walterbos, R. A. M., & Greenwalt, B. E. 1996, AJ, 112, 1429
Hoyle, F. 1965, Natur, 208, 111
Hunstead, R. W., Murdoch, H. S., & Shobbrook, R. R. 1978, MNRAS, 185, 149
Hurley-Walker, N., Callingham, J. R., Hancock, P. J., et al. 2017, MNRAS, 464, 1146
Hutchings, J. B., Gower, A. C., Ryneveld, S., & Dewey, A. 1996, AJ, 111, 2167
Ichinohe, Y., Werner, N., Simionescu, A., et al. 2015, MNRAS, 448, 2971
Intema, H. T., Jagannathan, P., Mooley, K. P., et al. 2017, A&A, 598, A78
Jauncey, D. L., Wright, A. E., Peterson, B. A., & Condon, J. J. 1978, ApJL, 219, L1
Jimenez-Gallardo, A., Massaro, F., Paggi, A., et al. 2021, ApJS, 252, 31
Jimenez-Gallardo, A., Massaro, F., Prieto, M. A., et al. 2020, ApJS, 250, 7
Johnson, S. D., Chen, H.-W., Straka, L. A., Schaye, J., & Cantalupo, S. 2018, ApJL, 869, L1
Johnston-Hollitt, M., Hunstead, R. W., & Corbett, E. 2008, A&A, 479, 1
Jones, D. H., Read, M. A., Saunders, W., et al. 2009, MNRAS, 399, 683
Jones, D. H., Saunders, W., Colless, M., et al. 2004, MNRAS, 355, 747
Joye, W. A., & Mandel, E. 2003, in ASP Conf. Ser. 295, Astronomical Data Analysis Software and Systems XII, ed. H. E. Payne, R. I. Jedrzejewski, & R. N. Hook (San Francisco, CA: ASP), 489
Ivezić, Ž., Kahn, S. M., Tyson, J. A., et al. 2019, ApJ, 873, 111
Kempner, J. C., Blanton, E. L., Clarke, T. E., et al. 2004, arXiv:astro-ph/0310263
Kenworthy, M. A., Snik, F., Keller, C. U., et al. 2018, Proc. SPIE, 10702E, 1070246
Killeen, N. E. B., Bicknell, G. V., & Carter, D. 1986, ApJ, 309, 45
Killeen, N. E. B., Bicknell, G. V., & Ekers, R. D. 1988, ApJ, 325, 180
Kinman, T. D., & Burbidge, E. M. 1967, ApJL, 148, L59
Kosiba, M., Peña-Herazo, H. A., Massaro, F., et al. 2023, A&A, 670, A171
Kuraszkiewicz, J., Wilkes, B. J., Atanas, A., et al. 2021, ApJ, 913, 134
Labiano, A., Barthel, P. D., O'Dea, C. P., et al. 2007, A&A, 463, 97
Lacy, M., Baum, S. A., Chandler, C. J., et al. 2020, PASP, 132, 035001
Laing, R. A., Riley, J. M., & Longair, M. S. 1983, MNRAS, 204, 151
Large, M. I., Mills, B. Y., Little, A. G., Crawford, D. F., & Sutton, J. M. 1981, MNRAS, 194, 693
Larionov, V. M., Jorstad, S. G., Marscher, A. P., Villata, M., & Raiteri, C. M. 2020, MNRAS, 492, 3829
Law-Green, J. D. B., Leahy, J. P., Alexander, P., et al. 1995, MNRAS, 274, 939
Lehnert, M. D., Miley, G. K., Sparks, W. B., et al. 1999, ApJS, 123, 351
Liu, T., Tozzi, P., Tundo, E., et al. 2013, A&A, 549, A143
Liu, T., Tozzi, P., Tundo, E., et al. 2015, ApJS, 216, 28
Longair, M. S. 1970, MNRAS, 150, 155
Longair, M. S., Best, P. N., & Rottgering, H. J. A. 1995, MNRAS, 275, L47
Ly, C., De Young, D., & Bechtold, J. 2005, ApJ, 618, 609
Lynds, C. R. 1967, ApJ, 147, 837
Lynds, C. R., Stockton, A. N., & Livingston, W. C. 1965, ApJ, 142, 1667
Madrid, J. P., Chiaberge, M., Floyd, D., Sparks, W. B., & Macchetto, D. 2006, ApJS, 164, 307
Marchesini, E. J., Paggi, A., Massaro, F., et al. 2019, A&A, 631, A150
Marchesini, E. J., Paggi, A., Massaro, F., et al. 2020, A&A, 638, A128
Marenbach, G., & Appenzeller, I. 1982, A&A, 108, 95
Marshall, H. L., Gelbord, J. M., Schwartz, D. A., et al. 2011, ApJS, 193, 15
Martel, A. R., Baum, S. A., Sparks, W. B., et al. 1999, ApJS, 122, 81
Maselli, A., Forman, W. R., Jones, C., Kraft, R. P., & Perri, M. 2022, ApJS, 262, 51
Massaro, F., Álvarez Crespo, N., D'Abrusco, R., et al. 2016, Ap&SS, 361, 337
Massaro, F., Chiaberge, M., Grandi, P., et al. 2009a, ApJL, 692, L123
Massaro, F., Giommi, P., Tosti, G., et al. 2008a, A&A, 489, 1047
Massaro, F., Harris, D. E., & Cheung, C. C. 2011, ApJS, 197, 24
Massaro, F., Harris, D. E., Chiaberge, M., et al. 2009b, ApJ, 696, 980
Massaro, F., Harris, D. E., Tremblay, G. R., et al. 2010, ApJ, 714, 589
Massaro, F., Harris, D. E., Tremblay, G. R., et al. 2013, ApJS, 206, 7
Massaro, F., Missaglia, V., Stuardi, C., et al. 2018, ApJS, 234, 7
Massaro, F., Tramacere, A., Cavaliere, A., Perri, M., & Giommi, P. 2008b, A&A, 478, 395
Massaro, F., Tremblay, G. R., Harris, D. E., et al. 2012, ApJS, 203, 31
Massaro, F., White, S. V., García-Pérez, A., et al. 2023, ApJS, 265, 32
Mauch, T., Murphy, T., Buttery, H. J., et al. 2003, MNRAS, 342, 1117
McCarthy, P. J., Baum, S. A., & Spinrad, H. 1996, ApJS, 106, 281
McCarthy, P. J., Miley, G. K., de Koff, S., et al. 1997, ApJS, 112, 415
McCarthy, P. J., Spinrad, H., & van Breugel, W. 1995, ApJS, 99, 27
McCollough, M. L., & Rots, A. H. 2005, in ASP Conf. Ser. 347, Astronomical Data Analysis Software and Systems XIV, ed. P. Shopbell, M. Britton, & R. Ebert (San Francisco, CA: ASP), 478
McMullin, J., Diamond, P., McPherson, A., et al. 2020, Proc. SPIE, 11445, 1144512
McNamara, B. R., & Nulsen, P. E. J. 2007, ARA&A, 45, 117
McNamara, B. R., & Nulsen, P. E. J. 2012, NJPh, 14, 055023
Mingo, B., Hardcastle, M. J., Ineson, J., et al. 2017, MNRAS, 470, 2762
Missaglia, V., Massaro, F., Capetti, A., et al. 2019, A&A, 626, A8
Moretti, A., Campana, S., Tagliaferri, G., et al. 2004, Proc. SPIE, 5165, 232
Morganti, R. 2017, FrASS, 4, 42
Morton, D. C., & Tritton, K. P. 1982, MNRAS, 198, 669
O'Dea, C. P., Baum, S. A., & Stanghellini, C. 1991, ApJ, 380, 66
Oh, K., Koss, M., Markwardt, C. B., et al. 2018, ApJS, 235, 4
Oke, J. B. 1974, ApJS, 27, 21
Oke, J. B., & Gunn, J. E. 1983, ApJ, 266, 713
Owen, F. N., & Rudnick, L. 1976, ApJL, 205, L1
Owers, M. S., Couch, W. J., & Nulsen, P. E. J. 2009, ApJ, 693, 901
Paggi, A., Massaro, F., D'Abrusco, R., et al. 2013, ApJS, 209, 9
Parisi, P., Masetti, N., Rojas, A. F., et al. 2014, A&A, 561, A67
Peña-Herazo, H. A., Amaya-Almazán, R. A., Massaro, F., et al. 2020, A&A, 643, A103
Peña-Herazo, H. A., Massaro, F., Chavushyan, V., et al. 2022, A&A, 659, A32
Peterson, B. A., & Bolton, J. G. 1972, ApJL, 173, L19
Privon, G. C., O'Dea, C. P., Baum, S. A., Axon, D. J., & Kharb, P. 2008, ApJS, 175, 423
Quintana, H., & Ramirez, A. 1995, ApJS, 96, 343
Ramos Almeida, C., Tadhunter, C. N., Inskip, K. J., et al. 2011, MNRAS, 410, 1550
Roming, P. W. A., Kennedy, T. E., Mason, K. O., et al. 2005, SSRv, 120, 95
Sandage, A. 1978, AJ, 83, 904

Sbarufatti, B., Falomo, R., Treves, A., & Kotilainen, J. 2006, A&A, 457, 35
Sejake, P. K., White, S. V., Heywood, I., et al. 2023, MNRAS, 518, 4290
Simpson, C., Clements, D. L., Rawlings, S., & Ward, M. 1993, MNRAS, 262, 889
Simpson, C., Rawlings, S., & Lacy, M. 1999, MNRAS, 306, 828
Spinrad, H., Marr, J., Aguilar, L., & Djorgovski, S. 1985, PASP, 97, 932
Springob, C. M., Haynes, M. P., Giovanelli, R., & Kent, B. R. 2005, ApJS, 160, 149
Stickel, M., & Kuehr, H. 1994, A&AS, 105, 67
Stocke, J. T., Penton, S., Harvanek, M., Neely, W. A., & Blades, J. C. 1998, AJ, 115, 451
Storchi-Bergmann, T., Wilson, A. S., Mulchaey, J. S., & Binette, L. 1996, A&A, 312, 357
Stuardi, C., Missaglia, V., Massaro, F., et al. 2018, ApJS, 235, 32
Sun, M. 2009, ApJ, 704, 1586
Tadhunter, C. N., Morganti, R., di Serego-Alighieri, S., Fosbury, R. A. E., & Danziger, I. J. 1993, MNRAS, 263, 999
Taylor, M. B. 2005, in ASP Conf. Ser. 347, Astronomical Data Analysis Software and Systems XIV, ed. P. Shopbell, M. Britton, & R. Ebert (San Francisco, CA: ASP), 29
Teague, P. F., Carter, D., & Gray, P. M. 1990, ApJS, 72, 715
Thompson, D. J., Djorgovski, S., & de Carvalho, R. 1990, PASP, 102, 1235
Tingay, S. J., Goeke, R., Bowman, J. D., et al. 2013, PASA, 30, e007
Tozzi, P., Moretti, A., Tundo, E., et al. 2014, A&A, 567, A89
Tritton, K. P. 1972, MNRAS, 158, 277
Tundo, E., Moretti, A., Tozzi, P., et al. 2012, A&A, 547, A57
Urry, P. 1995, PASP, 107, 803
Wayth, R. B., Lenc, E., Bell, M. E., et al. 2015, PASA, 32, e025
Wegner, G., Bernardi, M., Willmer, C. N. A., et al. 2003, AJ, 126, 2268
Wenger, M., Ochsenbein, F., Egret, D., et al. 2000, A&AS, 143, 9
Werner, M. W., Murphy, D. W., Livingston, J. H., Gorjian, V., & Jones, D. L. 2012, ApJ, 759, 86
White, S. V., Franzen, T. M. O., Riseley, C. J., et al. 2020a, PASA, 37, e017
White, S. V., Franzen, T. M. O., Riseley, C. J., et al. 2020b, PASA, 37, e018
Whiteoak, J. B. 1972, AuJPh, 25, 233
Wilkes, B. J., Kuraszkiewicz, J., Haas, M., et al. 2013, ApJ, 773, 15
Wills, D., & Parker, E. A. 1966, MNRAS, 131, 503
Worrall, D. M. 2009, A&ARv, 17, 1
Worrall, D. M., & Birkinshaw, M. 2017, MNRAS, 467, 2903
Wright, E. L., Eisenhardt, P. R. M., Mainzer, A. K., et al. 2010, AJ, 140, 1868
Wright, A. E., Jauncey, D. L., Peterson, B. A., & Condon, J. J. 1977, ApJL, 211, L115
Wright, A. E., Peterson, B. A., Jauncey, D. L., & Condon, J. J. 1979, ApJ, 229, 73
Yates, M. G., Miller, L., & Peacock, J. A. 1989, MNRAS, 240, 129
Yee, H. K. C., & Green, R. F. 1983, BAAS, 15, 957
Young, A. J., Wilson, A. S., Tingay, S. J., & Heinz, S. 2005, ApJ, 622, 830
Younis, S., Meaburn, J., & Stewart, P. 1985, A&A, 147, 178